

THE ROLE OF MAJOR MERGERS AND NUCLEAR STAR FORMATION IN NEARBY OBSCURED QUASARS

DONGYAO ZHAO¹, LUIS C. HO^{1,2}, YULIN ZHAO^{1,2}, JINYI SHANGGUAN^{1,2,3}, AND MINJIN KIM^{4,5}
(Dated: Accepted ??, Received ??)

¹The Kavli Institute for Astronomy and Astrophysics, Peking University, 5 Yiheyuan Road, Haidian District, Beijing 100871, China

²Department of Astronomy, School of Physics, Peking University, 5 Yiheyuan Road, Haidian District, Beijing 100871, China

³Max-Planck-Institut für extraterrestrische Physik, Gießenbachstr. 1, D-85748 Garching, Germany

⁴Department of Astronomy and Atmospheric Sciences, Kyungpook National University, Daegu 41566, Republic of Korea

⁵Korea Astronomy and Space Science Institute, Daedeokdae-ro 776, Yuseong-gu, Daejeon 34055, Republic of Korea

ABSTRACT

We investigate the triggering mechanism and the structural properties of obscured luminous active galactic nuclei from a detailed study of the rest-frame *B* and *I* *Hubble Space Telescope* images of 29 nearby ($z \approx 0.04 - 0.4$) optically selected type 2 quasars. Morphological classification reveals that only a minority (34%) of the hosts are mergers or interacting galaxies. More than half (55%) of the hosts contain regular disks, and a substantial fraction (38%), in fact, are disk-dominated ($B/T \lesssim 0.2$) late-type galaxies with low Sérsic indices ($n < 2$), which is characteristic of pseudo bulges. The prevalence of bars in the spiral host galaxies may be sufficient to supply the modest fuel requirements needed to power the nuclear activity in these systems. Nuclear star formation seems to be ubiquitous in the central regions, leading to positive color gradients within the bulges and enhancements in the central surface brightness of most systems.

Keywords: galaxies: evolution — galaxies: formation — galaxies: active — galaxies: bulges — galaxies: photometry — quasars: general

1. INTRODUCTION

The ubiquitous presence of supermassive black holes in the centers of galaxies and the tight correlations between black hole mass and bulge stellar mass (Magorrian et al. 1998; Kormendy & Ho 2013) and velocity dispersion (Ferrarese & Merritt 2000; Gebhardt et al. 2000) have often been attributed to a close connection between the growth of the central black hole (through accretion) and the growth of the host galaxy (through star formation). The exact nature of this connection, however, is still under debate. In this regard, active galactic nuclei (AGNs) are of great importance to understand the physical link between black holes and their host galaxies, as AGNs are powered by intense accretion of material onto the central black hole. Strong outflows from AGNs can quench star formation efficiently, and may be responsible for establishing the empirical correlations between black hole mass and host galaxy properties (e.g., Di Matteo et al. 2005; Springel et al. 2005).

One of the most crucial but yet unknown factors on clarifying the role of nuclear activity in the coevolution of black holes and their hosts is how AGNs are triggered. For AGNs with low to moderate luminosities (e.g., Seyfert galaxies with bolometric luminosities $L_{\text{bol}} \lesssim 10^{45}$ erg s⁻¹), observational and theoretical studies suggest

that various internal processes can trigger mass accretion to the central black hole (e.g., Hopkins & Hernquist 2009; Hopkins et al. 2014). However, these mechanisms are insufficient to explain the ignition of more powerful AGNs with $L_{\text{bol}} > 10^{45}$ erg s⁻¹. It seems unlikely that the gas reservoir on kpc scales can lose sufficient angular momentum to feed luminous quasars (Jogee 2006).

In numerical simulations, gas-rich major mergers are suggested as a promising mechanism to trigger luminous AGNs (e.g., Hopkins et al. 2008; Alexander & Hickox 2012). The morphological signatures of major mergers, such as close pairs, double nuclei, disturbed morphologies, tidal tails, and shells and bridges are expected to be visible up to $\sim 0.5 - 1.5$ Gyr after the merger. Given that the AGN lifetime is thought to be $\lesssim 100$ Myr (Martini & Weinberg 2001; Yu & Tremaine 2002; Martini 2004), the features of morphological disturbance should be observable in their host galaxies if luminous AGNs are triggered by gas-rich major mergers.

A number of observational studies have examined the morphologies of the host galaxies of luminous AGNs to test the major-merger scenario. A high frequency of distortions in the morphologies of AGN host galaxies has been reported in a number of studies using quasars selected from various methods (e.g., radio quasars: Ramos

Almeida et al. 2011, 2012; optically unobscured quasars: Veilleux et al. 2009), seemingly consistent with the conventional hypothesis. On the other hand, there are no shortage of studies that reach the opposite conclusion, that major mergers play only an insignificant role in triggering luminous AGNs (e.g., radio quasars: Dunlop et al. 2003; Floyd et al. 2004; X-ray quasars: Cisternas et al. 2011; Villforth et al. 2014; optically unobscured quasars: Mechtley et al. 2016).

According to the gas-rich major-merger scenario, luminous AGNs should be highly obscured during the early stages of the merger because of the enhanced concentration of gas and dust from the progenitor galaxies. In the aftermath of the merger event, these highly obscured, luminous AGNs—classified as “type 2” quasars—should be morphologically highly disturbed. When the obscuration clears and “type 1” quasars emerge toward the late stages of the evolution, it is unclear the extent to which the morphological signatures of the merger process still remain visible. Thus, type 2 quasars are the more promising targets to test the role of gas-rich major mergers in triggering AGNs, and the overall major merger-driven framework of black hole-galaxy coevolution.

In terms of morphological studies of AGN host galaxies, obscured sources enjoy another strong advantage compared with their unobscured counterparts because of their absence of a bright nucleus. The host galaxies of type 1 AGNs can be extraordinarily difficult to study because of the dominating influence of their strong central point source (e.g., Kim et al. 2008a,b, 2017; Mechtley et al. 2016). Even basic morphological classifications—not to mention of more quantitative structural parameters—can be challenging to obtain. By contrast, the nuclear obscuration of type 2 AGNs serves as a natural coronagraph to block the blinding nucleus, thereby affording a cleaner view of the detailed internal structures of the host galaxy.

Although various theoretical studies have long predicted the existence of obscured luminous AGNs, a limited number of type 2 quasars were known until large samples were discovered in the last decade (e.g., Zakamska et al. 2003; Martínez-Sansigre et al. 2005; Reyes et al. 2008; Alexandroff et al. 2016). At high redshifts ($z \approx 2$), Donley et al. (2018) demonstrate that major mergers play a dominant role in triggering and fuelling infrared-selected, luminous obscured AGNs. At intermediate redshifts ($z \approx 0.5$), morphological hints of interactions have also been found to be prevalent in the host galaxies of optically selected type 2 quasars (e.g., Villar-Martín et al. 2011; Wylezalek et al. 2016), further supporting the major merger scenario. However, the situation is less clear at lower redshifts ($z \lesssim 0.3$). Bessiere et al. (2012) reported a significant fraction (75%) of type

2 quasars showing evident features of morphological disturbance. Nevertheless, elliptical host galaxies were seen to be dominant ($\sim 70\%$) in type 2 samples by other studies, such as those of Zakamska et al. (2006) and Villar-Martín et al. (2012).

This work reports deep, high-resolution, rest-frame optical images obtained with the *Hubble Space Telescope* (*HST*) of a sample of 29 nearby ($z \approx 0.04 - 0.4$) type 2 quasars. Although the sample is modest, our observations represent the most extensive, detailed study to date of the host galaxies of obscured quasars in the local Universe. The *HST* images, taken in rest-frame *B* and *I*, enable us not only to investigate the morphological properties of the host galaxies but also to derive crude constraints on their stellar populations. We analyze the morphologies, photometric structures, colors, and stellar masses of the host galaxies, paying special emphasis on their bulges. We examine whether major mergers are causally connected to AGN activity.

The paper is organized as follows. Section 2 introduces the sample and describes the *HST* observations and data reduction. Section 3 presents the image analysis of the host galaxies, including morphological classification, structure decomposition, color map construction, and stellar mass estimation. Results and discussions are presented in Section 4. We summarize our main conclusions in Section 5. This work adopts the following cosmological parameters: $\Omega_m = 0.286$, $\Omega_\Lambda = 0.714$, and $H_0 = 69.6 \text{ km s}^{-1} \text{ Mpc}^{-1}$ (Bennett et al. 2014).

2. DATA

2.1. Sample Selection

Our type 2 quasars were originally selected to complement a matching study of low-redshift type 1 quasars selected from the Palomar-Green survey of Schmidt & Green (1983) to examine the evolutionary connection between these two populations, which will be reported in an upcoming paper. The comparison sample of Palomar-Green quasars consists of 87 objects with $z < 0.5$ (Borison & Green 1992). To this end, we randomly selected 87 type 2 quasars, matching the Palomar-Green sample in terms of redshift and [O III] $\lambda 5007$ luminosity, from the catalog of 887 type 2 quasars published by Reyes et al. (2008)¹. Type 2 quasars in this catalog were identified from the Sloan Digital Sky Survey (SDSS; York et al. 2000) Data Release 6 spectroscopic database (Adelman-McCarthy et al. 2008). Our selection assumes that type 2 quasars have the same intrinsic AGN luminosity as type

¹ Reyes et al. (2008) chose a luminosity cut of $L_{[\text{O III}]} > 10^{8.3} L_\odot$ to define type 2 quasars, but a fraction ($\sim 17\%$) of the sources in the catalog have luminosities below this limit because of recent recalibration of the SDSS spectrophotometry. In this study, we adopt the extinction-corrected [O III] luminosities of Kong & Ho (2018).

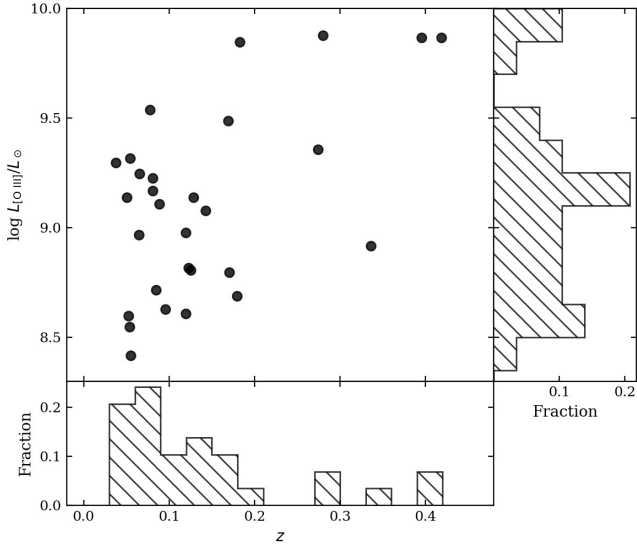


Figure 1. The distribution of extinction-corrected [O III] luminosity (Kong & Ho 2018) and redshift for our sample of 29 type 2 quasars. The sample is nearby (median $z \approx 0.1$) and has a median $\log(L_{[\text{O III}]} / L_{\odot}) = 9.11$.

1 quasars for a given $L_{[\text{O III}]}$, and that $L_{[\text{O III}]}$ is related to the bolometric luminosity of the AGN (Heckman et al. 2005; LaMassa et al. 2009; Dicken et al. 2014).

As the observations were conducted in the “snapshot” mode of *HST*, only $\sim 1/3$ of the original sample of type 2 quasars was observed successfully, yielding a sample of 29 objects (Table 1). The final sample spans a redshift range of 0.04 to 0.4, with a median value of $z = 0.12$, and extinction-corrected [O III] luminosities from $\log(L_{[\text{O III}]} / L_{\odot}) = 8.42$ to 9.88, with a median value of 9.11 (Fig. 1). The 29 objects have a similar distribution of redshifts, [O III] luminosities, and optical magnitudes as the original sample of 87 objects. They also match the distribution of these quantities in the parent catalog of Reyes et al. (2008) at $z < 0.5$.

2.2. *HST* WFC3 Observations

The observations were conducted using the WFC3 camera between November 2012 and July 2014 (proposal ID 12903; PI: Luis C. Ho). Each object was observed with a blue filter and a red filter using the UVIS or IR channel. The bandpasses were carefully chosen from the large suite of available WFC3 filters, with two considerations: to match approximately rest-frame *B* and *I*, and to avoid strong emission lines. Hereinafter, we denote the bluer filter (F438W, F475W, F555W) as B_{WFC3} and the redder filter (F814W, F105W, F110W, F125W) as I_{WFC3} .

For the UVIS channel, each quasar was observed with three long exposures, using the three-point dithering

pattern WFC3-UVIS-DITHER-LINE-3PT. For the IR channel, four long exposures were taken using the four-point dithering pattern WFC3-IR-DITHER-BOX-MIN. We used subarrays to minimize the readout time and buffer size, resulting in a field-of-view (FoV) of $67 \times 67 \text{ arcsec}^2$ and $40 \times 40 \text{ arcsec}^2$ for the IR and UVIS channels, respectively. These FoVs, which correspond to ~ 145 and 87 kpc at the median redshift of the sample, are sufficiently wide to cover the outskirts of the host galaxies for detecting extended features and to achieve accurate sky measurement. Total exposure times, which varied between 147 and 780 s, were set to reach a surface brightness limit of $\mu \approx 25 \text{ mag arcsec}^{-2}$, a depth that previous studies had demonstrated can yield robust detections of faint outer structures (e.g., Kim et al. 2008a; Greene et al. 2008; Jiang et al. 2011). Table 1 gives a summary of the observations.

2.3. Data Reduction

We use *AstroDrizzle* to combine the dithered images to generate cosmic ray-removed science images. The pixel scale is set to $0''.06$ for the IR channel and $0''.03$ for the UVIS channel so that it Nyquist samples the point-spread function (PSF), which has a full width at half maximum (FWHM) of $\sim 0''.13$ and $0''.07$ for the IR and UVIS channel, respectively. Fortunately, none of the central pixels near the nucleus was saturated. Although *AstroDrizzle* performs sky subtraction, further adjustments of the sky level were made during the two-dimensional (2-D) image fitting process using *GALFIT* (Peng et al. 2002, 2010; see Section 3.2.1).

A robust model of the PSF is crucial for accurate image decomposition, even for the hosts of type 2 AGNs. Ideally, the PSF can be constructed from bright stars observed simultaneously in the science images, but in general this is not possible in our program because of the relatively small FoV of our subarray images. While synthetic *TinyTim* (Krist et al. 2011) PSFs are commonly used as a substitute (e.g., Kim et al. 2017), our experience (Huang et al. 2019) indicates that empirical PSFs generated from stacked WFC3 images of multiple bright, unsaturated, isolated stars observed with the same filter, in the same dither pattern, but at different times perform significantly better than synthetic PSFs. Hence, our analysis uses a library of empirical PSFs of high signal-to-noise (S/N) created from stacking individual stars. The total number of stars used to generate the stacked PSF differs from filter to filter, with the average being a few tens.

3. ANALYSIS

We first inspect the images to visually classify the morphologies of the host galaxies. We then quantify their structural parameters through detailed 2-D image de-

Table 1. Observational Information

Object	z	D_L (Mpc)	$E(B - V)$ (mag)	$\log L_{[\text{O III}]}$ (L_\odot)	$\log L_{[\text{O III}]}$ (L_\odot)	Filter ($I_{\text{WFC3}}/B_{\text{WFC3}}$)	ExpTime (s)	ObsDate (yy-mm-dd)
(1)	(2)	(3)	(4)	(5)	(6)	(7)	(8)	(9)
SDSS J011935.63-102613.1	0.125	586	0.0371	8.43	8.81	F105W/F475W	147/780	2013-06-19
SDSS J074751.56+320052.1	0.280	1438	0.0700	8.95	9.88	F110W/F555W	147/780	2014-04-27
SDSS J075329.93+230930.7	0.336	1775	0.0633	8.59	8.92	F110W/F555W	147/780	2014-02-13
SDSS J075940.95+505024.0	0.054	243	0.0415	8.83	9.32	F814W/F438W	470/300	2013-09-09
SDSS J080252.92+255255.5	0.081	368	0.0329	8.86	9.23	F105W/F438W	147/705	2013-09-13
SDSS J080337.32+392633.1	0.065	295	0.0456	8.12	9.25	F105W/F438W	147/705	2014-01-12
SDSS J080523.29+281815.8	0.128	604	0.0476	8.62	9.14	F105W/F475W	147/570	2013-01-03
SDSS J081100.20+444216.3	0.183	888	0.0418	8.27	9.85	F105W/F475W	147/540	2013-01-21
SDSS J084107.06+033441.3	0.274	1404	0.0334	8.77	9.36	F110W/F555W	147/780	2014-01-21
SDSS J084344.99+354941.9	0.054	241	0.0360	8.14	8.55	F814W/F438W	260/320	2013-02-23
SDSS J090754.07+521127.5	0.085	386	0.0159	8.23	8.72	F105W/F438W	147/720	2013-03-12
SDSS J091819.66+235736.4	0.419	2303	0.0443	9.58	9.87	F125W/F555W	147/780	2013-04-14
SDSS J093625.36+592452.7	0.095	439	0.0200	8.35	8.63	F105W/F438W	147/780	2013-04-28
SDSS J103408.59+600152.2	0.050	225	0.0093	8.85	9.14	F814W/F438W	156/130	2013-10-09
SDSS J105208.19+060915.1	0.052	232	0.0310	8.20	8.60	F814W/F438W	325/390	2013-02-25
SDSS J110213.01+645924.8	0.077	352	0.0319	8.45	9.54	F105W/F438W	147/660	2013-08-03
SDSS J111015.25+584845.9	0.143	678	0.0096	8.88	9.08	F105W/F475W	147/780	2014-03-21
SDSS J113710.77+573158.7	0.395	2152	0.0097	9.61	9.87	F125W/F555W	147/780	2014-03-21
SDSS J115326.42+580644.5	0.064	290	0.0249	8.48	8.97	F105W/F438W	147/630	2014-03-19
SDSS J123804.81+670320.7	0.179	871	0.0190	8.26	8.69	F105W/F475W	147/780	2012-12-31
SDSS J125850.77+523913.0	0.055	246	0.0141	8.26	8.42	F814W/F438W	325/390	2013-01-11
SDSS J130038.09+545436.8	0.088	403	0.0180	8.94	9.11	F105W/F438W	147/660	2013-08-06
SDSS J133542.49+631641.5	0.169	816	0.0187	8.47	9.49	F105W/F475W	147/780	2013-08-10
SDSS J140541.21+402632.5	0.080	366	0.0135	8.78	9.17	F105W/F438W	147/660	2014-08-07
SDSS J140712.94+585120.4	0.170	823	0.0107	8.27	8.80	F105W/F475W	147/780	2013-05-29
SDSS J144038.09+533015.8	0.038	166	0.0115	8.94	9.30	F814W/F438W	188/132	2013-11-24
SDSS J145019.18-010647.4	0.120	559	0.0459	8.42	8.61	F105W/F475W	147/660	2013-06-15
SDSS J155829.36+351328.6	0.119	558	0.0246	8.77	8.98	F105W/F475W	147/540	2012-10-27
SDSS J162436.40+334406.7	0.122	573	0.0227	8.56	8.82	F105W/F475W	147/660	2013-09-07

Notes. Column (1): Object name. Column (2): Redshift. Column (3): Luminosity distance. Column (4): Galactic extinction. Column (5): Observed [O III] luminosity (Reyes et al. 2008). Column (6): Extinction-corrected [O III] luminosity (Kong & Ho 2018). Column (7): WFC3 filter. Column (8): Exposure time for I_{WFC3} and B_{WFC3} . Column (9): Date of observations.

composition. We generate color maps and color profiles, which enable us to derive stellar masses and explore the stellar population of the host galaxies.

3.1. Morphology Classification

The high resolution and sensitivity of the WFC3 images, coupled with the low redshifts of our sample, allow us to perform quite reliable visual classifications of the galaxy morphologies. We distinguish five broad types: merging/disturbed, unbarred spirals, barred spirals, lenticulars, and ellipticals. In this work, we regard spirals and lenticulars as disk galaxies, and we consider

spirals as late-type.

We summarize the classifications of the 29 objects as follows (Figure 2): 10 can be considered merging/disturbed because they exhibit obvious signs of interactions, distorted features, or otherwise reside in host galaxies in close pairs; three are found in unbarred and eight in barred spirals; five are hosted by lenticulars; and the remaining three are in ellipticals. The morphological type of each quasar can be found in Table 2.

Both the merging/disturbed system SDSS J162436.40+334406.7 and the lenticular galaxy SDSS

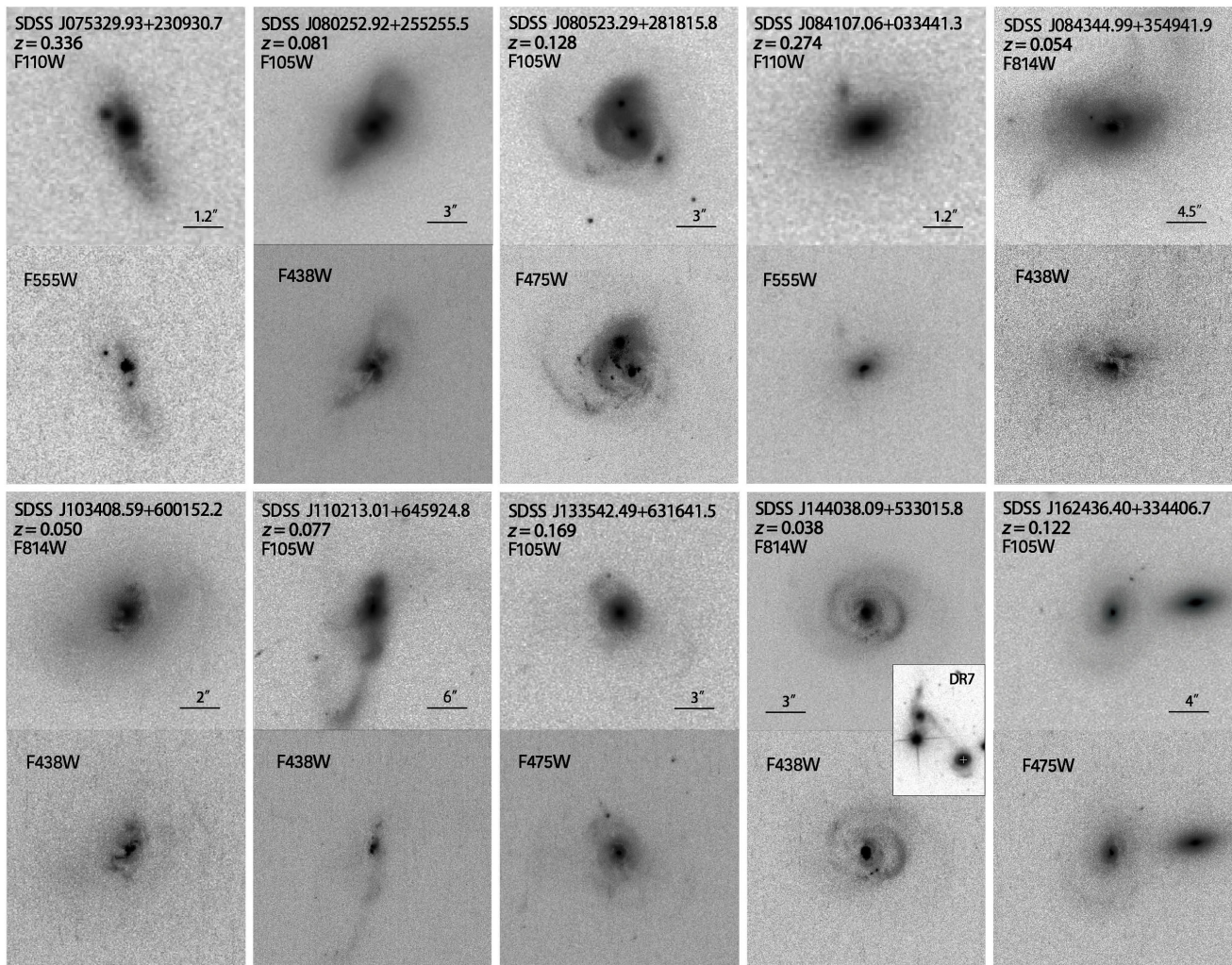


Figure 2. Morphological classifications of our sample. The objects are classified into five types: merging/disturbed, barred spiral, unbarred spiral, lenticular, and elliptical. The I_{WFC3} and B_{WFC3} images of each quasar are shown in the upper and lower panel, respectively, displayed using a logarithmic scale with the same FoV. The objects illustrated here have merging/disturbed host galaxies. A SDSS image with larger FoV is shown as an inset for SDSS J144038.09+533015.8 to demonstrate its interaction with another galaxy.

J093625.36+592452.7 have an apparent close companion. Based on available redshift measurements, the companion of SDSS J162436.40+334406.7 is genuinely associated with it, thus indeed constituting a merging system. However, the apparent companion of SDSS J093625.36+592452.7 is a foreground galaxy at $z = 0.04$. While the WFC3 images of SDSS J144038.09+533015.8 suggest that the host galaxy is an isolated spiral, a larger FoV SDSS image (see inset panel in Figure 2) reveals a long stellar bridge connecting the quasar to a disturbed companion, which prompted us to classify the host as merging/disturbed. We inspected large-FoV SDSS images for all the other objects in the sample and found no other examples of potential companions.

Surprisingly, the majority of the sample (55%) exhibit

unambiguous large-scale disks, with a significant fraction (38%) hosting clear late-type morphologies in the form of spiral arms and bars. Only approximately one-third of the host galaxies reside in close pairs or show obvious signatures of ongoing or recent interactions. If the ellipticals can be considered merger products, then in total $\sim 45\%$ of the sample are or have been associated with mergers of one type or another. Section 4.2 discusses the implications of these findings in relation to quasar triggering mechanisms.

Figure 3 shows the redshift distribution of the host galaxies with different morphological types. The galaxies with disks and morphologically disturbed features generally concentrate toward lower redshifts ($z \approx 0.1$) than those classified as ellipticals (median $z \approx 0.4$). Have ex-

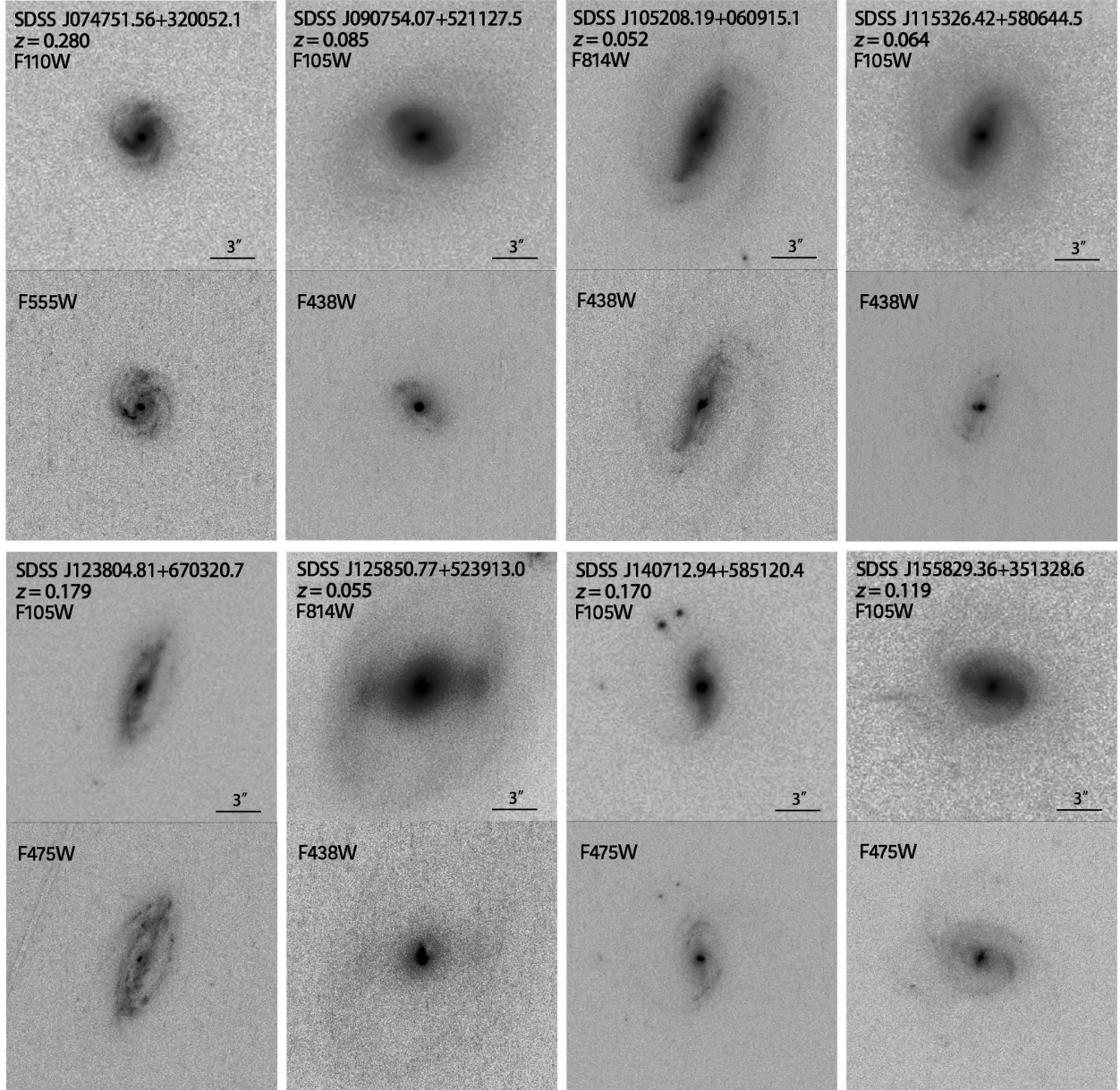


Figure 2 (Cont.). Host galaxies with morphology of barred spirals.

tended features of low surface brightness been missed in these more distant objects?

To test whether surface brightness dimming is the main cause of the classification of the elliptical galaxies, we use the FERENGI code (Barden et al. 2008) to generate mock, redshifted images of galaxies using the actual observed images of lower redshift objects. To match the luminosity of quasars with elliptical hosts ($\log L_{[\text{O III}]} / L_{\odot} = 8.88, 9.58, 9.61$), we choose nearby counterparts with similar [O III] luminosities covering the range of extended morphologies (merging/disturbed, barred and unbarred spirals, lenticulars). The code takes into account the cosmological corrections for size, surface brightness, bandpass

shifting, and k -correction. FERENGI treats the cosmological evolution of the stellar population, crudely parameterizing the luminosity evolution as $dM/dz = -1$ (Ilbert et al. 2005). We assume that the mock high- z quasars are located at $z = 0.143$ and observed with the filter pair F475W/F105W, or at $z = 0.4$ and observed with the filter pair F555W/F125W.

In the set of simulated IR images (upper panel in Figure 4), many of the original morphological details are lost, and most of the galaxies would be incorrectly classified as ellipticals or lenticulars when viewed in F105W at $z = 0.143$ or in F125W at $z = 0.4$. However, the simulated UVIS F475W and F555W images do a much

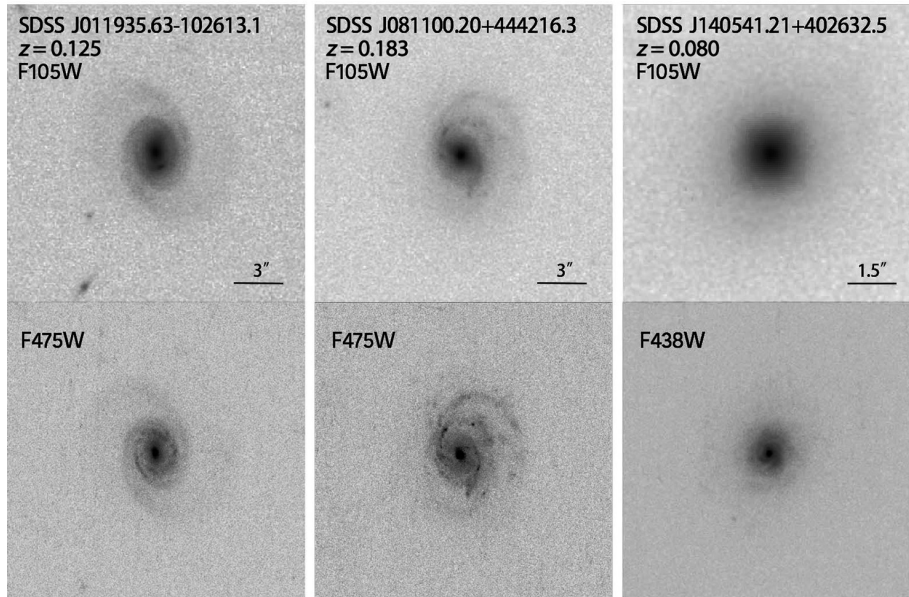


Figure 2 (Cont.). Host galaxies with morphology of unbarred spirals.

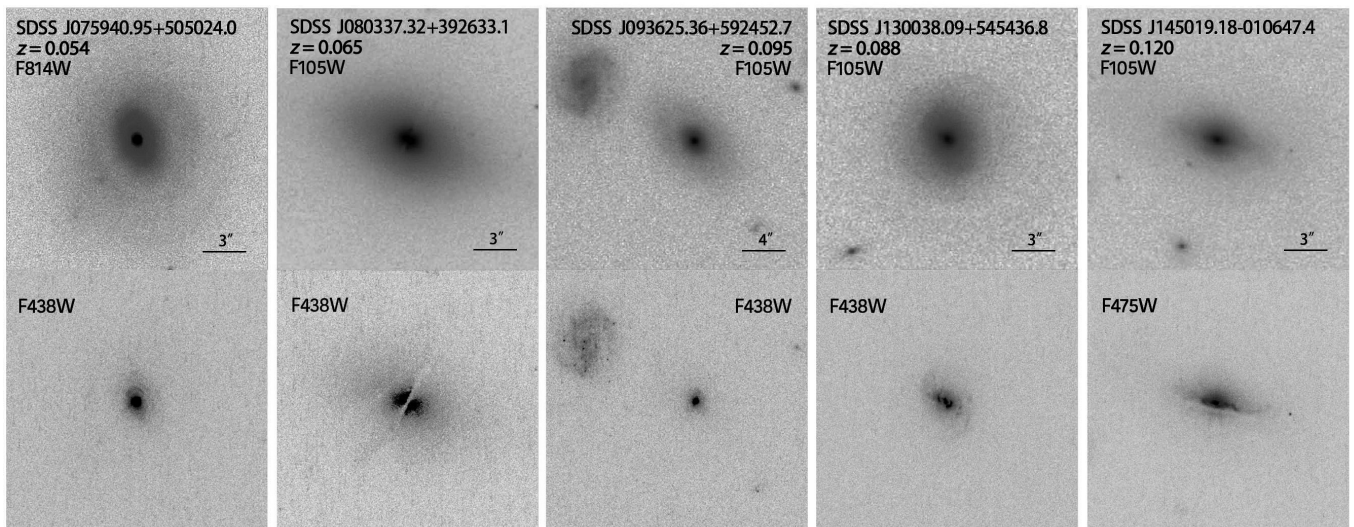


Figure 2 (Cont.). Host galaxies with morphology of lenticulars.

better job in retaining the original structural information (bottom panel in Figure 4). Therefore, so long as images in both filters are available, the morphological classification is unlikely to be biased in our study. We conclude that the morphological classifications of the three elliptical hosts in our sample should be secure.

3.2. Structural Decomposition

We analyze the images using GALFIT V3.0 (Peng et al. 2010), a non-linear least-squares fitting code that uses Levenberg-Marquardt minimization to decompose the major structural components of galaxies. We allow GALFIT to generate its own σ (weight) image. The sky value is fixed to a constant determined from the

average background value of five source-free 150×150 pixel² regions, and the uncertainty of the sky is the standard deviation of the five measurements. The sky measurement is measured separately for each image of each filter. To minimize contamination from nearby sources, we masked all objects beyond 1.5 times the Kron radius² from the target quasar. Additionally, objects that are more than 2.5 mag fainter than the target quasar are masked out regardless of their position because they will hardly affect the fit for the pri-

² We use the following definition of Kron radius: $R_{\text{Kron}} = 2.5r_1$, where r_1 is the first moment of the light distribution (Kron 1980; Bertin & Arnouts 1996). For an elliptical light distribution, this is, strictly speaking, the semi-major axis.

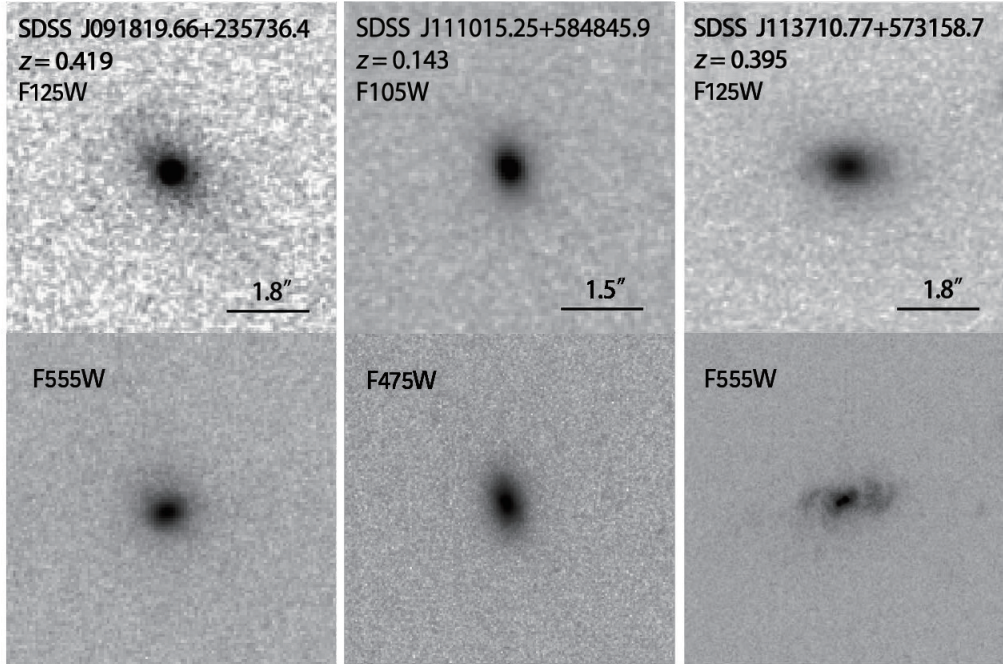


Figure 2 (Cont.). Host galaxies with morphology of ellipticals.

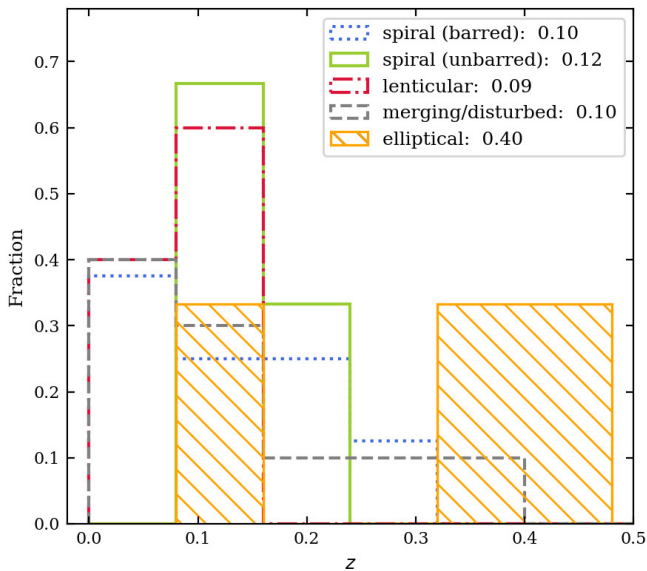


Figure 3. Redshift distribution of host galaxies with different morphologies. The median redshift of each subsample is shown. Quasars with elliptical morphology have higher redshift ($z \approx 0.4$) than others ($z \approx 0.1$).

mary target. Unmasked close companions are simultaneously fit with the target galaxy. Prominent dust lanes and regions need to be masked in some objects (e.g., SDSS J080337.32+392633.1, J145019.18–010647.4, and J084344.99+354941.9).

3.2.1. Best-fit Models

We fit bulges with the Sérsic (1968) profile. We set an upper limit of $n = 8$ for the Sérsic index, which is close to the largest values seen in the most luminous ellipticals (e.g., Kormendy et al. 2009). Moreover, values larger than $n = 8$ are often associated with poor model fits (Barden et al. 2012). We adopt an exponential profile ($n = 1$) for the disk component. Spiral arms, when clearly visible, are modeled by coordinate rotation and bending modes provided by GALFIT V3.0 (Peng et al. 2010; additional examples can be found in Gao & Ho 2017 and Gao et al. 2019). Three lenticular galaxies (SDSS J075940.95+505024.0, J093625.36+592452.7, and J130038.09+545436.8) exhibit an inner lens. Gao & Ho (2017, see also Gao et al. 2018) demonstrate that neglecting inner lenses will bias the derived bulge parameters significantly. Therefore, we model the inner lens as an independent component with either a Sérsic or an exponential profile, depending on which gives the better fit.

The bar, when present, needs to be properly included to avoid incurring large errors on the derived properties of the bulge (Laurikainen et al. 2004, 2005; Gadotti 2008; Gao & Ho 2017). Following common practice (e.g., Freeman 1966; de Jong 1996), we adopt a fixed Sérsic $n = 0.5$ profile for the bar component. Figure 5 demonstrates the effect of the bar component for one of the objects in the sample. Without a bar component (middle panel), the size, brightness, and ellipticity of the bulge appear to be substantially overestimated due to the influence of the bar. The poor match of the ellipticity profile as well as the large residuals at $r \approx 2''$ – $4''$ further attest to the

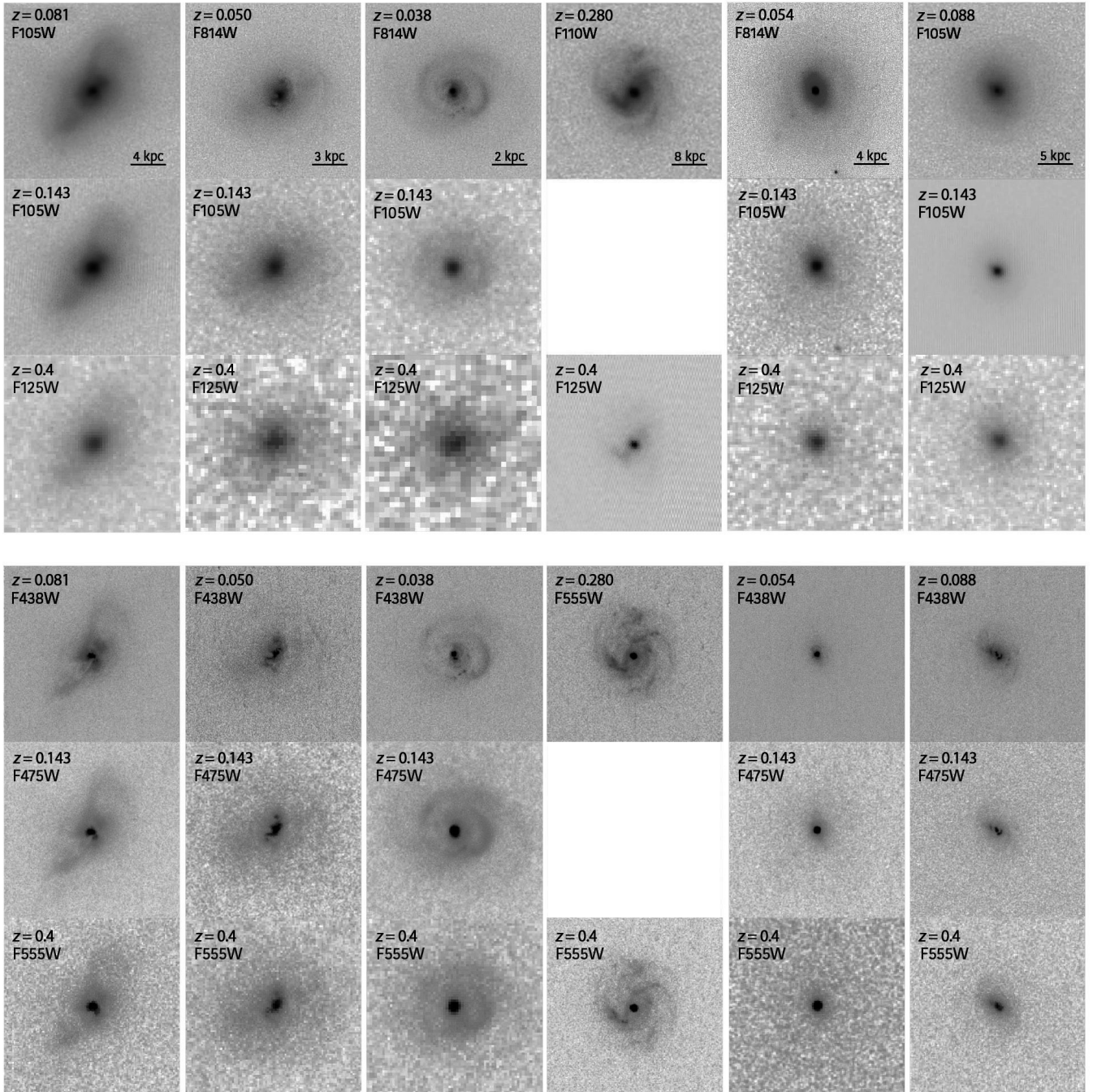


Figure 4. Simulated galaxies created with the FERENGI code after shifting low- z quasars with their original filters (first row in the upper/bottom panel) to $z = 0.143$ with F105W/F475W filter (second row in the upper/bottom panel) and to $z = 0.4$ with F125W/F555W filter (third row in the upper/bottom panel). Note that the quasar at $z = 0.28$ can only be shifted to $z = 0.4$, so that no simulated image exists at $z = 0.143$.

inadequacy of the model without a bar.

For host galaxies classified as merging/disturbed, especially for those with substantial disturbance, the bulge component cannot always be distinguished clearly from the other irregular components. We take as the bulge the prominent central component, which is usually well fit with a single Sérsic profile (with $n \leq 8$). We use Fourier modes (Peng et al. 2010) to model asymmetric structures such as lopsided features and tidal tails.

Although the active nucleus should be deeply obscured in type 2 quasars, a fraction of its light can still scatter out (Antonucci & Miller 1985) and thereby modify the innermost light profile of the galaxy. A significant fraction of our sample requires an additional compact, nuclear component—modeled as an unresolved PSF component—to achieve a satisfactory fit for the bulge. Absent the nuclear component, the Sérsic index of the bulge can reach unrealistically high values that are inconsistent with the values expected for the morphological types of the host galaxies. An example is illustrated in the right panel of Figure 5. The three-component (bulge, bar, and disk) model yields a bulge Sérsic index of $n = 4.63$, which would be unprecedented for such an obviously late-type galaxy (e.g., Balcells et al. 2003; Vika et al. 2015). The origin of the large Sérsic index is clear: the very central region contains a sharp spike, which has the effect of mimicking a large n . After including an additional nucleus component (left panel of Figure 5), the bulge Sérsic index drops to a much more reasonable value of $n = 2.08$. This suggests that accounting for a nuclear component, probably due to scattered light, is essential to deriving accurate photometric properties of the bulge. A nuclear component seems to be required in 14 objects, of which six are spirals, two are ellipticals, and six are merging/disturbed hosts. The nucleus typically contributes $\lesssim 10\%$ of the total brightness of the galaxy (average of 8% in I_{WFC3} and 9% in B_{WFC3}). Note that, with absolute magnitudes of -18 to -21 , these central components are unlikely to be nuclear star clusters, which have typical absolute magnitudes of $M_I \approx -10$ to -14 (Böker et al. 2002).

The I_{WFC3} -band images are significantly deeper than the B_{WFC3} -band images. The redder bandpass is also intrinsically more sensitive to the dominant, older stellar component of the host, and, of course, is less affected by dust extinction. We first determine the best-fit model using the I_{WFC3} -band image. Then we fix all structural parameters of the sub-components (e.g., R_e , position angle, ellipticity, central position) to solve only for their brightnesses in the B_{WFC3} band. The mask and sky level of the B_{WFC3} -band image are determined in the same manner as the I_{WFC3} -band image.

The best-fit models from the I_{WFC3} -band images for the sample are given in Appendix A, and the final param-

eters are summarized in Table 2. The fits are generally good, with reduced $\chi^2 \approx 1$. Quasars that are classified as barred and unbarred spirals tend to have less centrally concentrated ($n \lesssim 2$) and smaller ($R_e \lesssim 0.6''$) bulges, with B/T generally less than 0.2. In contrast, the ellipticals and bulges of lenticular and merging/disturbed hosts have much more concentrated ($n > 2$), larger ($R_e > 0.6''$), and more dominant ($B/T > 0.2$) spheroids. We will discuss in detail the implication of the bulge properties with different morphologies in Section 4.1.

3.2.2. Uncertainties of Best-fit Parameters

Three main factors contribute to the uncertainties of the structural parameters: uncertainties in sky determination, variations of the PSF, and assumptions of the model construction. Uncertainties in sky determination do not affect much components of high surface brightness, such as the bulge, but they do impact the lower surface brightness, extended structures, such as the disk and tidal features. To study the impact of sky determination, we repeat the fits by perturbing the sky level one standard deviation above and below the mean value. The impact of PSF variations was assessed by stacking different combinations of stars to generate variants of the empirical PSFs, and then repeating the fits.

By far the largest source of uncertainty comes from the assumptions that unavoidably need to be made when constructing simplified 2-D models to fit the intrinsically complex structure of galaxies. This problem was recently investigated by Gao & Ho (2017), who studied the impact of including various morphological components (e.g., inner/outer lenses, bars, disk breaks, spiral arms) on the derived parameters of galaxy bulges. Gao & Ho (2017) showed that inner lenses and bars present the dominant source of uncertainty for the bulge parameters, whereas outer spiral arms have a marginally effect. Therefore, for the disk galaxies in our sample, we explicitly treat bars and, if present, lenses and nuclei. For completeness, we also include spiral arms, even though they are not essential for the robust measurements of the bulge. The best-fit models reproduce properly the observed surface brightness profiles of most galaxies. Following Gao & Ho (2017), we adopt an average uncertainty of 0.1 mag for the bulge luminosity, and 10% for other structural parameters of the bulge. Ellipticals are obviously less complex, but our single-component fits may be an oversimplification (Huang et al. 2013). We nominally assign their uncertainties half of the above uncertainties adopted for bulges. The model uncertainty for the hosts with merging/disturbed morphologies is difficult to ascertain. For concreteness, we simply assume that their uncertainties are twice those for bulges. The final uncertainties for the structural parameters are the quadrature sum of the uncertainties from the sky, PSF, and model

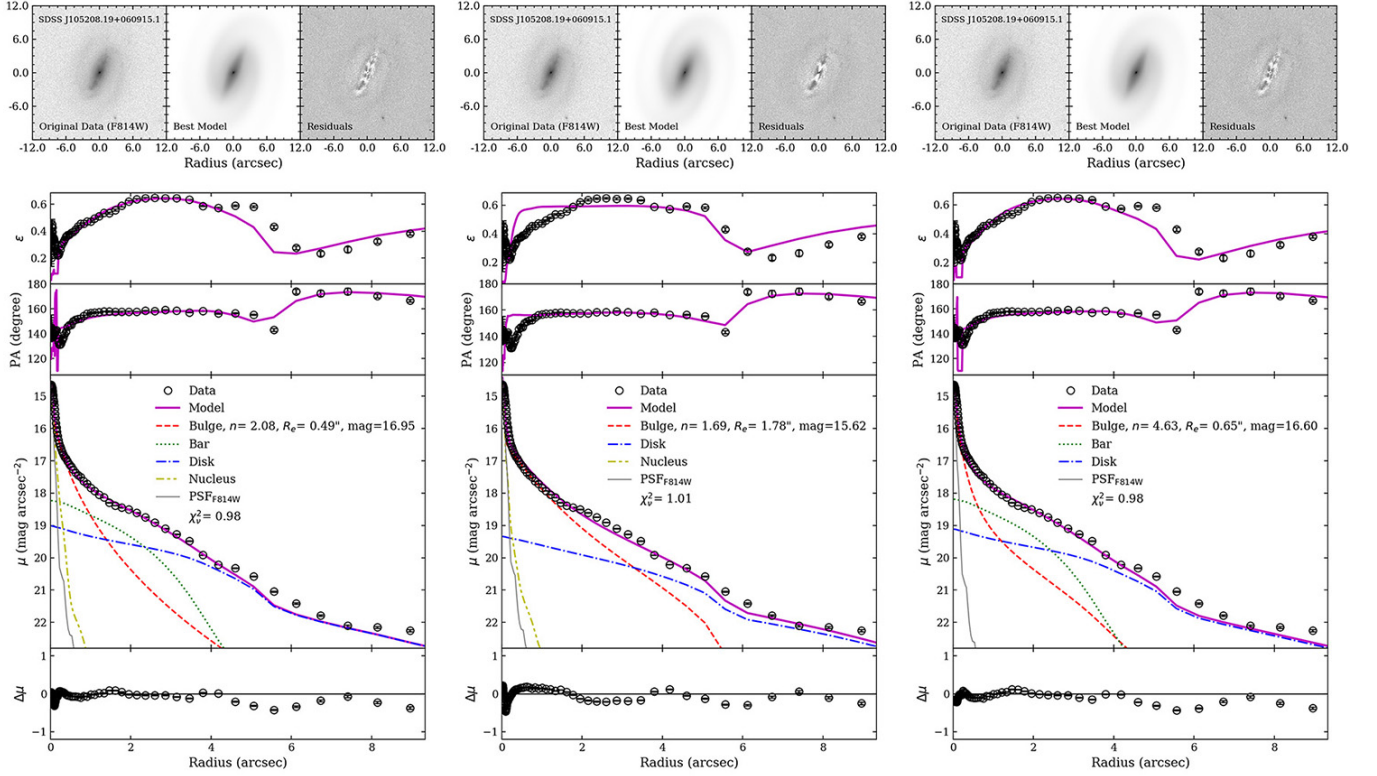


Figure 5. Comparison of the best-fit parameters for different models of the bulge of the spiral host galaxy of SDSS J105208.19+060915.1, to show the effects of the bar and AGN nucleus. For each panel, the original I_{WFC3} image, 2-D model, and residual images are illustrated in the upper panel, and the radial distributions of ellipticity, position angle, surface brightness, and residuals are shown in the bottom panel. The PSF is plotted with arbitrary amplitude. Left panel illustrates the best-fit model that includes both the bar and the nucleus. The overall structure is well-modeled, and the parameters have reasonable values. Middle panel shows the results from the model without a bar component. Although the Sérsic index n appears reasonable, R_e and magnitude of bulge are overestimated; moreover, the ellipticity and residual profiles show the necessity of an additional component around $2''$ – $4''$. The fit without a nucleus component, shown in the right panel, gives a bulge Sérsic index that is larger than expected for late-type galaxies. Therefore, both a bar and a nucleus are essential to obtain reasonable structural parameters for this object.

decomposition.

3.3. Colors

The *HST* observations were designed specifically to provide at least rudimentary color information with the filter combination of rest-frame B and I . In view of the possibility that the central region of the galaxy might be contaminated mildly by scattered light from the AGN (Section 3.2.1), we perform the color analysis on the images after subtracting the best-fit nucleus component, if present. We can generate color images in a straightforward manner for the six targets that were observed with the same (UVIS) detector. The majority (23/29), however, were observed with two detectors with different pixel scales and spatial resolutions. We rebin the UVIS images to match the pixel scale of the IR images, and we convolve the images taken in one filter with the cor-

responding PSF of the other filter. The color maps are generated by $(B - I)_{\text{WFC3}} = -2.5 \log(f_{B_{\text{WFC3}}}/f_{I_{\text{WFC3}}}) + ZP_{B_{\text{WFC3}}} - ZP_{I_{\text{WFC3}}}$, where $f_{B_{\text{WFC3}}}$ and $f_{I_{\text{WFC3}}}$ are the counts in B_{WFC3} and I_{WFC3} , respectively, and $ZP_{B_{\text{WFC3}}}$ and $ZP_{I_{\text{WFC3}}}$ are the corresponding zero points. We apply the IRAF task `ellipse` to the color images to derive radial color profiles.

Figure 6 gives the color maps and color profiles. For each object, the upper panel shows the B_{WFC3} image, the I_{WFC3} image, and the $(B - I)_{\text{WFC3}}$ color map. The color radial profile is shown in the bottom panel. We will discuss the results in Section 4.1.

3.4. Bulge Stellar Masses

We convert the I_{WFC3} magnitude of the bulge ($M_{I,\text{bul}}$) to the bulge stellar mass (M_{bul}) using a mass-to-light ratio (M/L) inferred from the rest-frame $(B - I)$ color.

Table 2. Best-fit Parameters of Host Galaxies

Object	I_{WFC3}										E_{WFC3}									
	Filter	n_{bulge}	$R_{e,\text{bulge}}$ (")	Bulge (mag)	Disk (mag)	Bar (mag)	Nucleus (mag)	Total (mag)	B/T	Filter	Bulge (mag)	Disk (mag)	Bar (mag)	Nucleus (mag)	Total (mag)	Morphology				
(1)	(2)	(3)	(4)	(5)	(6)	(7)	(8)	(9)	(10)	(11)	(12)	(13)	(14)	(15)	(16)	(17)				
J011935	F105W	1.85 ^{+0.19} _{-0.20}	0.78 ^{+0.08} _{-0.08}	17.03 ^{+0.09} _{-0.09}	16.58 ^{+0.01} _{-0.01}	19.52 ^{+0.09} _{-0.03}	15.97	0.27	F475W	19.94 ^{+0.12} _{-0.11}	18.85 ^{+0.02} _{-0.02}	21.42 ^{+0.13} _{-0.09}	18.51	spiral (unbarred)				
J074751	F110W	0.53 ^{+0.11} _{-0.12}	0.09 ^{+0.04} _{-0.05}	18.83 ^{+0.10} _{-0.10}	16.98 ^{+0.01} _{-0.01}	18.70 ^{+0.03} _{-0.02}	16.62	0.13	F555W	20.92 ^{+0.11} _{-0.11}	19.18 ^{+0.02} _{-0.01}	21.65 ^{+0.03} _{-0.02}	18.89	spiral (barred)				
J075329	F110W	2.25 ^{+0.46} _{-0.47}	0.80 ^{+0.16} _{-0.16}	18.20 ^{+0.19} _{-0.19}	19.66 ^{+0.01} _{-0.03}	20.05 ^{+0.02} _{-0.02}	17.95	0.79	F555W	21.05 ^{+0.22} _{-0.21}	22.31 ^{+0.03} _{-0.02}	23.98 ^{+0.14} _{-0.01}	20.76	merging				
J075940 ^b	F814W	1.04 ^{+0.12} _{-0.20}	0.12 ^{+0.02} _{-0.02}	16.60 ^{+0.09} _{-0.09}	15.48 ^{+0.03} _{-0.03}	16.38 ^{+0.01} _{-0.01}	14.85	0.20	F438W	18.17 ^{+0.09} _{-0.09}	17.62 ^{+0.06} _{-0.07}	18.84 ^{+0.05} _{-0.04}	16.91	lenticular				
J080252	F105W	4.53 ^{+0.91} _{-0.92}	1.65 ^{+0.33} _{-0.33}	14.16 ^{+0.16} _{-0.14}	14.76 ^{+0.02} _{-0.00}	13.67	0.63	F438W	17.25 ^{+0.17} _{-0.17}	17.69 ^{+0.01} _{-0.01}	16.70	merging				
J080337	F105W	4.57 ^{+0.46} _{-0.46}	4.82 ^{+0.52} _{-0.52}	13.68 ^{+0.07} _{-0.07}	15.16 ^{+0.04} _{-0.04}	13.43	0.80	F438W	18.68 ^{+0.15} _{-0.15}	17.19 ^{+0.03} _{-0.03}	16.94	lenticular				
J080523 ^a	F105W	2.22 ^{+0.49} _{-0.49}	0.87 ^{+0.18} _{-0.18}	16.87 ^{+0.17} _{-0.17}	15.40 ^{+0.00} _{-0.00}	18.05 ^{+0.05} _{-0.07}	15.15	0.21	F475W	20.23 ^{+0.22} _{-0.21}	17.91 ^{+0.04} _{-0.02}	19.94 ^{+0.01} _{-0.09}	17.79	merging				
J081100	F105W	4.03 ^{+0.48} _{-0.48}	0.41 ^{+0.05} _{-0.06}	16.97 ^{+0.12} _{-0.10}	16.07 ^{+0.02} _{-0.01}	15.61	0.18	F475W	20.05 ^{+0.11} _{-0.10}	18.30 ^{+0.02} _{-0.03}	18.10	spiral (unbarred)				
J084107	F110W	4.08 ^{+0.85} _{-0.87}	1.46 ^{+0.30} _{-0.30}	17.07 ^{+0.17} _{-0.17}	19.65 ^{+0.19} _{-0.06}	17.07	1.00	F555W	19.39 ^{+0.19} _{-0.19}	23.30 ^{+0.02} _{-0.08}	19.39	merging				
J084344	F814W	3.98 ^{+0.89} _{-1.23}	4.18 ^{+1.57} _{-1.39}	14.67 ^{+0.25} _{-0.42}	15.12 ^{+0.10} _{-0.24}	14.12	0.60	F438W	16.97 ^{+0.18} _{-0.17}	17.66 ^{+0.08} _{-0.08}	16.51	disturbed				
J090754	F105W	1.89 ^{+0.21} _{-0.21}	0.24 ^{+0.02} _{-0.02}	16.42 ^{+0.09} _{-0.08}	15.49 ^{+0.01} _{-0.01}	16.29 ^{+0.01} _{-0.01}	19.46 ^{+0.48} _{-0.20}	14.77	0.22	F438W	19.39 ^{+0.10} _{-0.11}	18.44 ^{+0.10} _{-0.11}	19.56 ^{+0.06} _{-0.05}	23.24 ^{+0.12} _{-0.05}	17.82	spiral (barred)				
J091819	F125W	1.79 ^{+0.14} _{-0.25}	1.10 ^{+0.08} _{-0.07}	18.75 ^{+0.08} _{-0.06}	19.26 ^{+0.14} _{-0.06}	18.75	1.00	F555W	20.95 ^{+0.06} _{-0.06}	21.01 ^{+0.15} _{-0.01}	20.95	elliptical				
J093625 ^b	F105W	2.92 ^{+0.29} _{-0.31}	0.17 ^{+0.02} _{-0.02}	16.81 ^{+0.09} _{-0.09}	16.01 ^{+0.01} _{-0.01}	17.56 ^{+0.02} _{-0.04}	15.42	0.28	F438W	19.77 ^{+0.10} _{-0.10}	19.39 ^{+0.10} _{-0.11}	17.90 ^{+0.01} _{-0.02}	17.51	lenticular				
J103408	F814W	3.42 ^{+0.79} _{-1.55}	3.99 ^{+1.10} _{-1.56}	14.45 ^{+0.35} _{-1.52}	14.82 ^{+0.64} _{-0.64}	13.87	0.59	F438W	16.31 ^{+0.17} _{-0.16}	17.35 ^{+0.11} _{-0.11}	15.96	disturbed				
J105208	F814W	2.08 ^{+0.22} _{-0.22}	0.49 ^{+0.05} _{-0.05}	16.95 ^{+0.09} _{-0.09}	15.39 ^{+0.03} _{-0.03}	16.37 ^{+0.03} _{-0.05}	19.59 ^{+0.05} _{-0.07}	14.85	0.14	F438W	19.48 ^{+0.10} _{-0.10}	17.38 ^{+0.06} _{-0.07}	18.86 ^{+0.07} _{-0.04}	20.49 ^{+0.07} _{-0.05}	17.01	spiral (barred)				
J110213 ^a	F105W	2.06 ^{+0.41} _{-0.47}	1.58 ^{+0.32} _{-0.32}	15.11 ^{+0.16} _{-0.16}	15.01 ^{+0.01} _{-0.00}	16.57 ^{+0.16} _{-0.03}	14.30	0.48	F438W	19.08 ^{+0.19} _{-0.19}	17.76 ^{+0.00} _{-0.01}	20.44 ^{+0.08} _{-0.09}	17.48	merging				
J111015	F105W	4.56 ^{+0.24} _{-0.45}	0.13 ^{+0.01} _{-0.01}	17.94 ^{+0.05} _{-0.04}	17.94	1.00	F475W	19.59 ^{+0.07} _{-0.07}	19.59	elliptical				
J113710	F125W	5.97 ^{+0.38} _{-0.40}	0.97 ^{+0.08} _{-0.08}	17.16 ^{+0.05} _{-0.05}	17.16	1.00	F555W	19.81 ^{+0.06} _{-0.06}	19.81	elliptical				
J115326	F105W	1.75 ^{+0.19} _{-0.27}	0.19 ^{+0.02} _{-0.02}	16.66 ^{+0.08} _{-0.08}	15.34 ^{+0.01} _{-0.01}	16.54 ^{+0.01} _{-0.01}	18.04 ^{+0.26} _{-0.02}	14.81	0.18	F438W	19.31 ^{+0.10} _{-0.10}	17.95 ^{+0.07} _{-0.07}	19.81 ^{+0.09} _{-0.07}	20.22 ^{+0.01} _{-0.04}	17.54	spiral (barred)				
J123804	F105W	1.31 ^{+0.13} _{-0.13}	0.20 ^{+0.02} _{-0.02}	19.12 ^{+0.10} _{-0.10}	16.93 ^{+0.00} _{-0.00}	16.91 ^{+0.00} _{-0.00}	16.10	0.06	F475W	22.17 ^{+0.12} _{-0.12}	20.13 ^{+0.02} _{-0.00}	18.83 ^{+0.02} _{-0.04}	18.51	spiral (barred)				
J125850	F814W	1.62 ^{+0.16} _{-0.33}	0.61 ^{+0.06} _{-0.06}	16.57 ^{+0.11} _{-0.09}	14.88 ^{+0.05} _{-0.05}	16.43 ^{+0.03} _{-0.02}	14.48	0.15	F438W	18.85 ^{+0.12} _{-0.12}	17.24 ^{+0.13} _{-0.15}	19.60 ^{+0.16} _{-0.14}	16.92	spiral (barred)				
J130038 ^b	F105W	3.82 ^{+0.42} _{-0.41}	0.71 ^{+0.09} _{-0.08}	15.90 ^{+0.09} _{-0.10}	15.79 ^{+0.01} _{-0.02}	16.86 ^{+0.09} _{-0.09}	14.90	0.40	F438W	18.43 ^{+0.10} _{-0.10}	19.85 ^{+0.65} _{-1.85}	19.16 ^{+0.09} _{-0.09}	17.80	lenticular				
J133542	F105W	3.01 ^{+0.61} _{-0.61}	1.69 ^{+0.34} _{-0.34}	16.06 ^{+0.16} _{-0.16}	18.58 ^{+0.05} _{-0.01}	16.06	1.00	F475W	18.33 ^{+0.19} _{-0.18}	21.93 ^{+0.17} _{-0.03}	18.33	disturbed				
J140541	F105W	1.69 ^{+0.17} _{-0.20}	0.50 ^{+0.05} _{-0.05}	15.83 ^{+0.09} _{-0.08}	16.16 ^{+0.02} _{-0.01}	17.60 ^{+0.07} _{-0.01}	15.19	0.45	F438W	18.16 ^{+0.10} _{-0.10}	18.65 ^{+0.09} _{-0.10}	19.70 ^{+0.11} _{-0.03}	17.63	spiral (unbarred)				
J140712	F105W	1.86 ^{+0.19} _{-0.19}	0.19 ^{+0.02} _{-0.02}	17.28 ^{+0.09} _{-0.09}	16.80 ^{+0.01} _{-0.01}	17.44 ^{+0.03} _{-0.03}	15.94	0.29	F475W	19.66 ^{+0.13} _{-0.10}	19.00 ^{+0.04} _{-0.04}	20.39 ^{+0.04} _{-0.04}	18.35	spiral (barred)				
J144038	F814W	2.04 ^{+0.42} _{-0.45}	0.19 ^{+0.04} _{-0.05}	16.35 ^{+0.17} _{-0.16}	14.34 ^{+0.03} _{-0.03}	17.96 ^{+0.16} _{-0.04}	14.18	0.14	F438W	17.54 ^{+0.18} _{-0.18}	16.09 ^{+0.04} _{-0.04}	18.64 ^{+0.03} _{-0.03}	15.84	merging				
J145019	F105W	4.22 ^{+0.54} _{-0.50}	1.81 ^{+0.38} _{-0.38}	15.38 ^{+0.14} _{-0.12}	16.88 ^{+0.36} _{-0.20}	15.14	0.80	F475W	18.51 ^{+0.12} _{-0.12}	18.89 ^{+0.05} _{-0.06}	17.93	lenticular				
J155829	F105W	0.80 ^{+0.08} _{-0.09}	0.31 ^{+0.03} _{-0.03}	18.10 ^{+0.09} _{-0.09}	16.25 ^{+0.01} _{-0.01}	17.11 ^{+0.03} _{-0.03}	19.48 ^{+0.07} _{-0.00}	15.72	0.11	F475W	19.99 ^{+0.10} _{-0.10}	18.30 ^{+0.05} _{-0.05}	19.82 ^{+0.05} _{-0.05}	21.67 ^{+0.13} _{-0.03}	17.89	spiral (barred)				
J162436	F105W	1.93 ^{+0.39} _{-0.41}	0.79 ^{+0.16} _{-0.16}	16.84 ^{+0.18} _{-0.18}	15.88 ^{+0.01} _{-0.00}	19.14 ^{+0.08} _{-0.02}	15.51	0.29	F475W	19.27 ^{+0.20} _{-0.20}	18.59 ^{+0.04} _{-0.04}	21.31 ^{+0.12} _{-0.05}	18.13	merging				

Notes. Column (1): Galaxy name. Column (2): Filter used, corresponding to I_{WFC3} . Column (3)–(8): Best-fit GALFIT parameters. Column (9): Total magnitude of the host, excluding the nucleus, if present. Column (10): B/T ratio. Column (11): Filter used, corresponding to E_{WFC3} . Column (12)–(15): Best-fit GALFIT parameters. Column (16): Total magnitude of the host, excluding the nucleus, if present. Column (17): Morphological classification.

^aThe magnitude of the disk in Column (6) and (13) is the sum of the magnitudes of all the components except the bulge and nucleus component.

^bThis galaxy has an inner lens; the magnitude given in Column (7) and (14) refer to the lens instead of the bar.

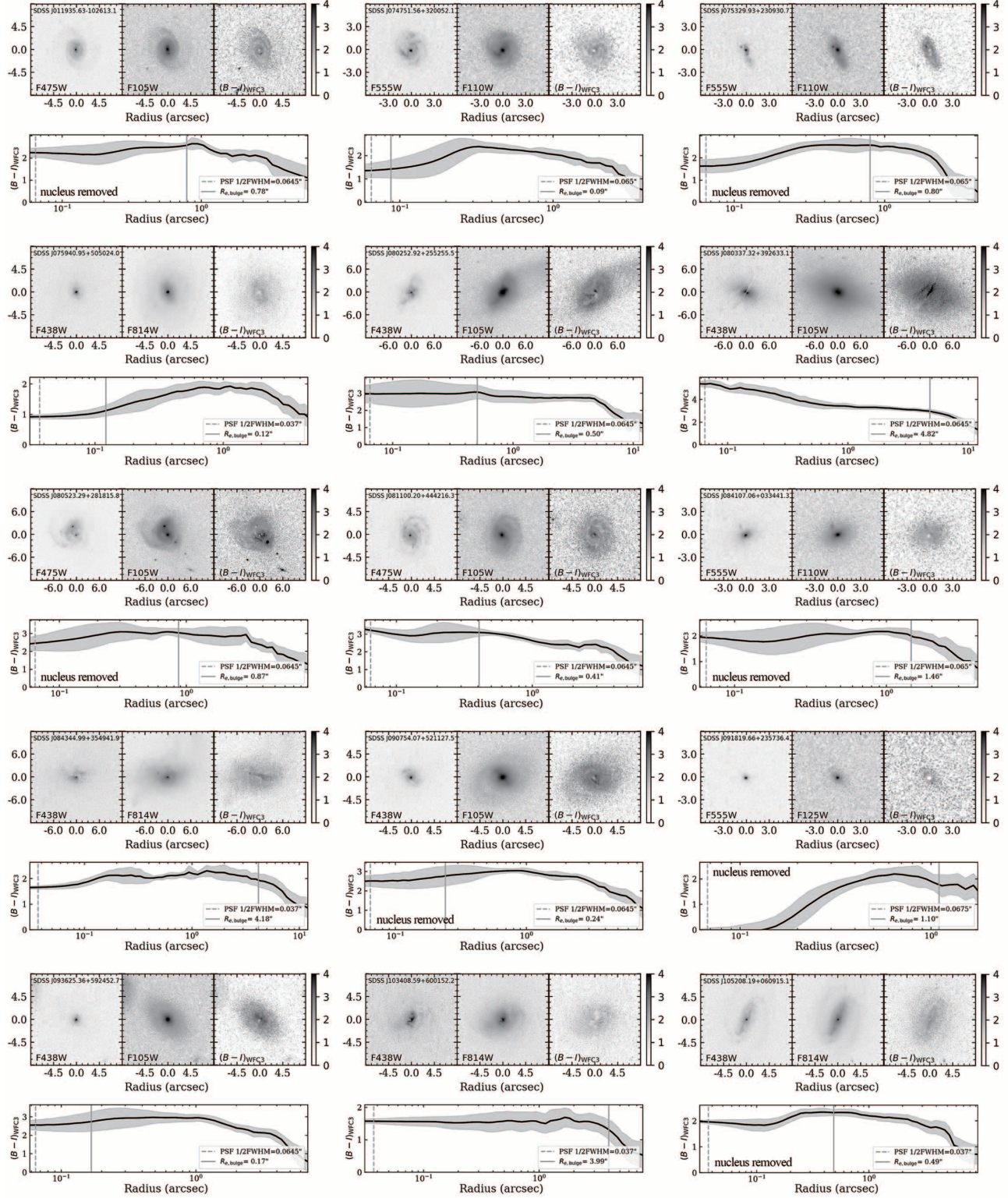


Figure 6. Color maps and color profiles of the host galaxies. The original I_{WFC3} and B_{WFC3} images are rebinned onto the same pixel scale and convolved with each other's PSF. A nucleus component, if needed from the best-fit GALFIT model, has been removed. The upper panel shows the B_{WFC3} image, the I_{WFC3} image, and the $(B-I)_{WFC3}$ color map, with color bar on the far right end. The bottom panel shows the color radial profile (black solid curve) measured from the center of the galaxy out to 1.5 times the Kron radius. The grey shaded area shows the root-mean-square scatter. The dashed vertical line marks 1/2 FWHM of the PSF, and the vertical solid line shows the best-fit effective radius of the bulge.

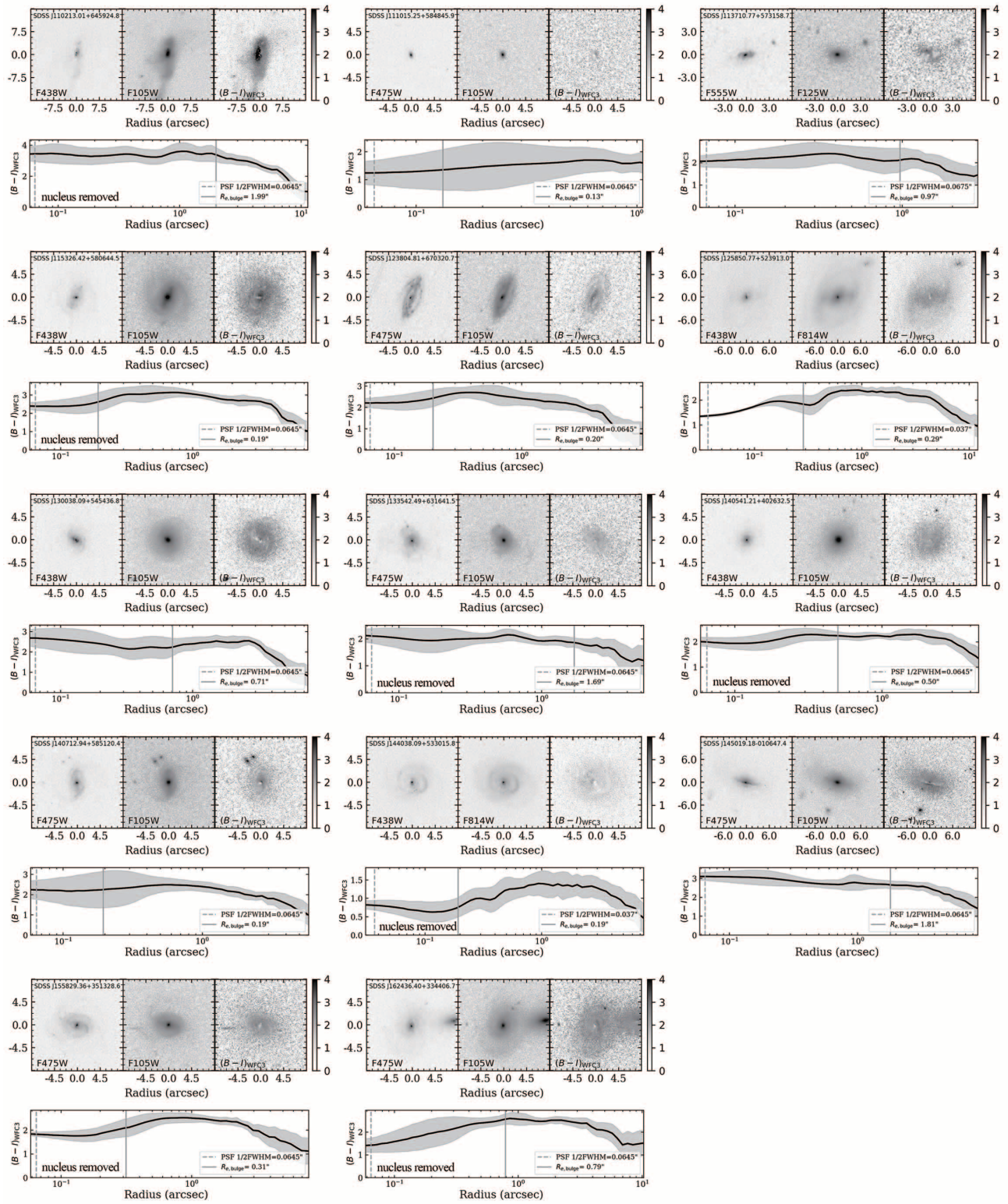


Figure 6 (Cont.). Color maps and color profiles of host galaxies.

Adopting the color-based conversion from [Bell & de Jong \(2001\)](#),

$$\log\left(\frac{M_{\text{bul}}}{M_{\odot}}\right) = -0.4(M_{I,\text{bul}} - M_{I,\odot}) + 0.439(B - I) - 0.594, \quad (1)$$

where $M_{I,\odot} = 4.08$ is the I -band absolute magnitude of the Sun ([Binney & Merrifield 1998](#)). This relation assumes a [Kroupa \(2001\)](#) stellar initial mass function. The stellar masses have typical errors of ~ 0.1 dex due to uncertainties in stellar population ([Bell et al. 2003](#); [Conroy et al. 2009](#)).

We use the SDSS Data Release 7 (DR7) spectrum of each object to calculate the k -correction and the color conversion from the B_{WFC3} and I_{WFC3} filters to conventional B and I filters. Strictly speaking, the SDSS spectrum, taken using a $3''$ fiber, covers the central ~ 5.6 kpc of the host galaxy (for median $z \approx 0.1$), much larger than the size scale of the bulge. Nevertheless, we will use it and confirm later that the stellar mass derived from the spectrum well represents the bulge mass.

Note that the spectral range of the SDSS spectrum is not wide enough to cover the I_{WFC3} bandpass. We, therefore, derive the stellar spectrum by fitting the SDSS spectrum (see [Figure 7](#) for an example) with a [Bruzual & Charlot \(2003, BC03\)](#) stellar population synthesis model consisting of four stellar components with ages in the range $[0.04, 0.3]$, $[0.3, 1.0]$, $[0.0, 3.0]$, and 8.0 Gyr, assuming solar metallicity. Strong emission lines are excluded from the fit. Meanwhile, Galactic extinction is removed adopting $R_V = 3.1$ and the Milky Way extinction law of [Cardelli et al. \(1989\)](#). As previously noted, contamination from nuclear scattered light is not entirely negligible for 14 of the quasars. For consistency, a power-law continuum representing the AGN component is included in the fits for these objects. The SDSS spectra of 24 targets have sufficiently high S/N ($\gtrsim 15$) that their best-fit BC03 model yields a reduced $\chi^2 \approx 1$. For the remaining five objects with spectra of lower quality (S/N < 7), we simply adopt a model consisting of an old (10 Gyr) and a young (2.1 Gyr) population ([Canalizo & Stockton 2013](#)).

In view of the fact that the SDSS spectrum generally covers larger regions of the host galaxy than the scale of bulge, we consider the SDSS spectrum to be representative of the whole host galaxy and derive an alternative estimate of the bulge stellar mass. We first obtain the total stellar mass of the host galaxy (M_*) using its integrated I -band magnitude and $(B - I)$ color by [Equation 1](#), and then we attribute a fraction B/T thereof to the bulge ($M_{\text{bul},B/T}$). These alternative estimates of the bulge masses derived from B/T agree well with those derived from bulge magnitudes: $\langle \log M_{\text{bul}} - \log M_{\text{bul},B/T} \rangle = 0.03 \pm 0.16$ dex.

Another check on our stellar masses can be made using the subset of 19 objects that overlap with the MPA-JHU catalog³ of spectral measurements from SDSS DR7. The stellar masses in this catalog were derived from spectral energy distribution fits to the DR7 photometry⁴. The median total stellar masses from DR7 ($M_{*,\text{DR7}}$) agree well with our estimates: $\langle \log M_* - \log M_{*,\text{DR7}} \rangle = -0.01 \pm 0.13$ dex.

[Table 3](#) lists the stellar masses derived in this work. For simplicity, in the following discussion, we simply adopt the bulge masses (M_{bul}) estimated from [Equation \(1\)](#). We note that none of the conclusions of this paper depends on which of the two bulge masses we choose.

4. RESULTS AND IMPLICATIONS

4.1. Evidence of Nuclear Star Formation

Black hole accretion and star formation are often suggested to go hand in hand ([Springel et al. 2005](#); [Hopkins et al. 2006](#)), but the verdict from observations is somewhat mixed. While some studies of the stellar population of AGN host galaxies find nuclear and starburst activity to be broadly synchronized (e.g., [Tadhunter et al. 2011](#); [Bessiere et al. 2014, 2017](#)), others maintain that AGN activity significantly lags behind star formation (e.g., [Wild et al. 2010](#); [Canalizo & Stockton 2013](#)). The color information from this study provides some fresh insights into this issue, from the point of view of luminous, obscured quasars that should be experiencing both intense star formation and black hole growth.

The color maps shown in [Figure 6](#) illustrate that in most of the hosts the central regions of the bulge are generally bluer than their outer regions. This holds for most of the merging/disturbed hosts and most of the disk galaxies. The few that do not follow this trend may be affected by dust reddening (i.e. some of the disturbed systems and two of the lenticulars with prominent inner dust lanes). Consistent with the expected behavior of galaxies, almost all the global color profiles initially exhibit a negative color gradient in their outermost regions (become redder toward smaller radii). However, upon reaching the central regions, roughly on the scale of the effective radius of the bulge, most of the color profiles flatten or even turn over at smaller radii.

To quantify this effect, we derive the color gradients of the inner and outer regions of the host galaxies (see [Table 3](#)), and we directly compare them with a control sample of inactive galaxies measured in the same manner from the Carnegie-Irvine Galaxy Survey (CGS; [Ho et al. 2011](#)). The inner region is defined as the range from half of the PSF FWHM (to avoid possible AGN contamination, even after subtracting the nucleus) to the effective

³ www.mpa-garching.mpg.de/SDSS/DR7/

⁴ See details in www.mpa-garching.mpg.de/SDSS/DR7/mass.comp.

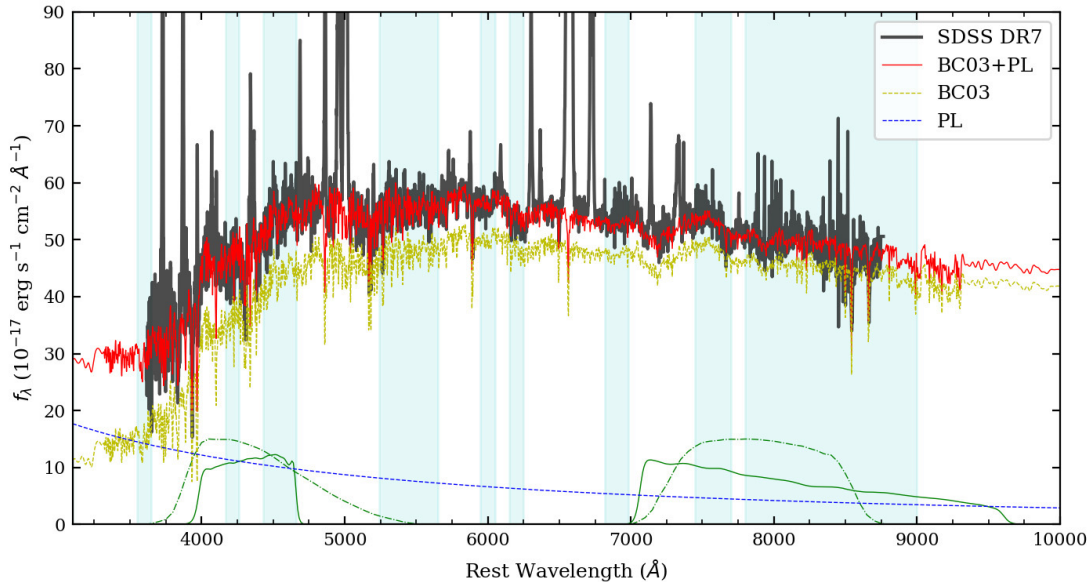


Figure 7. An example of fitting the rest-frame, Galactic extinction-corrected SDSS spectrum (black solid curve) of SDSS J105208.19+060915.1 to obtain a sufficiently broad stellar continuum. The shaded cyan areas show the parts of the spectrum used in our fits that avoid strong emission lines. The model consists of four BC03 stellar population synthesis components. A power-law AGN component is included to be consistent with the GALFIT fit. The red solid curve is the total best-fit continuum containing all BC03 components and the power law; the yellow dashed curve is the stellar component (linear sum of the four BC03 components); the blue dashed line is the power-law component. The bandpasses of the WFC3 filters are presented as green solid curves, and those of the B and I filters are shown as green dash-dotted curves.

radius of the bulge (R_e); the outer region extends between R_e and $2.5R_e$. Following Li et al. (2011), the color gradient, corrected for Galactic extinction, is calculated as the slope of the color profile, representing the change in color per dex in radius:

$$\nabla(\text{color})_{\text{in/out}} = \frac{(\text{color})_{r_1} - (\text{color})_{r_0}}{\log r_1 - \log r_0}, \quad (2)$$

where r_1 and r_0 correspond to R_e and 0.5 FWHM of PSF for the inner region, and $2.5R_e$ and R_e for the outer region. As in Li et al. (2011), color gradients larger than 0.1 are considered positive, between -0.1 and 0 are flat, and smaller than -0.1 are negative. A positive slope indicates that the galaxy is getting bluer toward the center.

Regardless of the sign of the outer color gradients, most of our objects exhibit *positive* inner $B - I$ color gradients. Figure 8 compares the inner color gradients of our sample, split by morphological types, relative to a comparison sample drawn from CGS (Li et al. 2011). The two samples are clearly different. Apart from two S0 hosts with central dust lanes, all the early-type hosts of type 2 quasars (ellipticals and S0s) have positive inner color gradients. By comparison, 85% of the ellipticals and 64% of the S0s in CGS have flat inner color profiles. The contrast is even more pronounced for spiral galaxies, for which *all* spiral AGN hosts have clearly positive

inner color gradients, whereas negative gradients characterize the majority (65 – 88%, depending on the exact morphological type) of the bulges of inactive spirals. Even merging/disturbed systems hosting type 2 quasars, whose environments expected to be dusty, mostly exhibit positive inner color gradients. The host galaxies of type 2 quasars have a preponderance of blue central regions compared to normal galaxies of similar Hubble type, consistent with enhanced ongoing or recent star formation.

Additionally, less direct but nevertheless compelling evidence for enhanced central star formation in type 2 quasars comes from inspection of the detailed structural parameters of the host galaxies. Figure 9 illustrates the distributions of Sérsic index (n) and bulge-to-total ratio (B/T) as a function of bulge stellar mass (M_{bul}) for the sample. Not unexpectedly, the merging/disturbed hosts (grey symbols) tend to have more massive ($M_{\text{bul}} \gtrsim 10^{10.5} M_{\odot}$), more prominent ($B/T \gtrsim 0.2$) bulges with relatively large Sérsic indices (median $n = 2.63$), akin to classical bulges and consistent with the expectation that major mergers build classical bulges (Kormendy & Kennicutt 2004; Fisher & Drory 2008). The undisturbed early types in the sample (lenticulars and ellipticals; red and orange symbols, respectively) span a wide range in mass, but their Sérsic indices are large (median $n = 4.02$), again consistent with classical bulges.

Table 3. Stellar Masses and Color Gradients

Object	$\log M_*$ (M_\odot)	$\log M_{\text{bul},B/T}$ (M_\odot)	$\log M_{\text{bul}}$ (M_\odot)	$\nabla(B-I)_{\text{in}}$	$\nabla(B-I)_{\text{out}}$	Morphology
(1)	(2)	(3)	(4)	(5)	(6)	(7)
J011935.63	10.71	10.29	10.45	0.64	-0.72	spiral (unbarred)
J074751.56	11.03	10.14	10.06	1.24	1.65	spiral (barred)
J075329.93	11.00	10.90	10.92	0.83	-2.99	merging
J075940.95	10.67	9.97	9.75	0.73	0.79	lenticular
J080252.92	11.27	11.07	11.10	0.63	-0.66	merging
J080337.32	11.30	11.20	11.16	-1.27	-3.91	lenticular
J080523.29	11.12	10.43	10.75	1.17	-0.86	merging
J081100.20	11.18	10.64	10.89	0.60	-1.65	spiral (unbarred)
J084107.06	11.03	11.03	11.03	0.64	-2.43	merging
J084344.99	11.05	10.83	10.79	0.07	-2.44	disturbed
J090754.07	10.92	10.26	10.23	0.90	1.29	spiral (barred)
J091819.66	10.26	10.26	10.26	1.70	-1.76	elliptical
J093625.36	10.28	9.73	10.11	1.15	1.17	lenticular
J103408.59	10.99	10.76	10.66	-0.10	-2.20	disturbed
J105208.19	10.65	9.81	9.97	0.20	-0.60	spiral (barred)
J110213.01	10.95	10.62	10.90	0.35	-2.57	merging
J111015.25	9.70	9.70	9.70	1.34	1.23	elliptical
J113710.77	10.91	10.91	10.91	0.39	-1.57	elliptical
J115326.42	10.56	9.82	9.79	1.02	1.48	spiral (barred)
J123804.81	10.93	9.73	10.01	1.52	0.13	spiral (barred)
J125850.77	10.96	10.12	10.05	0.75	0.82	spiral (barred)
J130038.09	10.86	10.46	10.30	0.48	0.63	lenticular
J133542.49	10.88	10.88	10.88	0.36	-1.47	disturbed
J140541.21	10.58	10.32	10.27	0.41	-0.05	spiral (unbarred)
J140712.94	10.97	10.44	10.43	1.69	1.54	spiral (barred)
J144038.09	11.01	10.14	9.94	-0.29	1.45	merging
J145019.18	11.14	11.04	11.10	0.03	-1.90	lenticular
J155829.36	10.71	9.76	9.64	0.59	1.06	spiral (barred)
J162436.40	10.99	10.46	10.38	1.21	-0.13	merging

Notes. Column (1): Galaxy name. Column (2): Total stellar mass of host galaxy. Column (3): Bulge mass calculated from M_* and B/T . Column (4): Bulge mass calculated from M/L ratio of Equation (1). Column (5): Color gradients of the galaxy inner regions. The units are Δmag per dex in radius (arcsec). Column (6): Color gradients of the galaxy outer regions. Column (7): Morphological classification.

The late-type hosts are strikingly different. Most of the barred and unbarred spirals (blue and green symbols) have bulges of lower mass ($M_{\text{bul}} \lesssim 10^{10.5} M_\odot$), lower prominence ($B/T \lesssim 0.2$), and characteristically lower Sérsic indices ($n \lesssim 2$). They conform to the typical properties of pseudo bulges (Kormendy & Kennicutt 2004; Fisher & Drory 2008).

The Kormendy relation (Kormendy 1977), an inverse correlation between the effective radius (R_e) of spheroids

and their surface brightness (μ_e) within R_e , provides a useful empirical tool to distinguish bulge types. At a given R_e , pseudo bulges have lower μ_e than classical bulges or elliptical galaxies (Kormendy & Kennicutt 2004; Gadotti 2009; Fisher & Drory 2010). Figure 10 (top) examines the Kormendy relation of our sample using best-fit parameters from the I_{WFC3} band. We fit the relation only for the classical bulges (i.e. ellipticals and the bulges of merging/disturbed and lenticular galaxies),

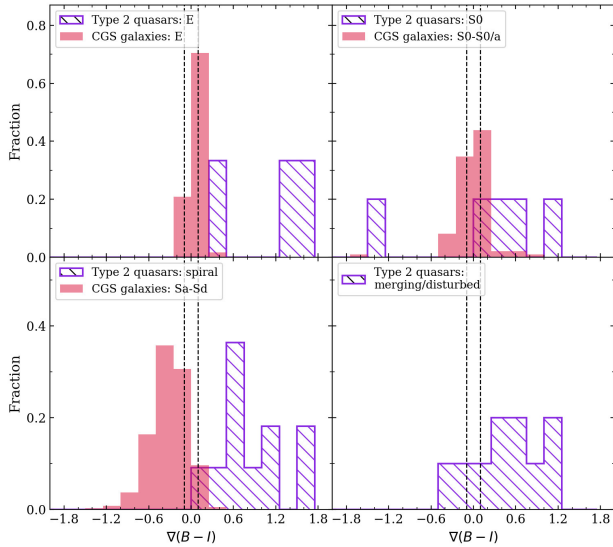


Figure 8. Color gradients of the inner regions (radius $< R_e$) of type 2 quasars (hatched purple histograms), divided by morphology. The inner gradients of normal (inactive) CGS galaxies with similar morphologies (Li et al. 2011) are shown for comparison as the filled red histograms; no CGS comparison is given for the merging/disturbed category. The vertical dashed lines in each panel mark the adopted boundaries for negative ($\nabla(B-I) < -0.1$), flat ($-0.1 \leq \nabla(B-I) \leq 0.1$), and positive ($\nabla(B-I) > 0.1$) color gradients. A positive color gradient means that the color becomes bluer toward the center. The central regions of most quasars have positive color gradients, opposite to the trend in normal galaxies.

which is denoted by the solid line. It is surprising that the late-type galaxies, which, as argued above, contain pseudo bulges, do *not* depart from the relation of classical bulges. This grossly deviates from the behavior of inactive galaxies, for which pseudo bulges scatter systematically below the locus of classical bulges and ellipticals. Why do pseudo bulges not appear in the Kormendy relation of type 2 quasar host galaxies? The simplest and most plausible explanation is that the bulge effective surface brightnesses have been enhanced because of excess light from recent or ongoing star formation. Together with the color gradients previously discussed, we conclude that the central regions of these obscured quasars have a characteristically young stellar population, presumably associated with a recent episode of star formation. A similar trend is also reported in the hosts of type 1 AGNs (Kim & Ho 2019).

4.2. Are Mergers Important for Triggering AGNs?

The role of mergers in governing AGN activity remains a vexingly controversial topic. From a theoretical point of

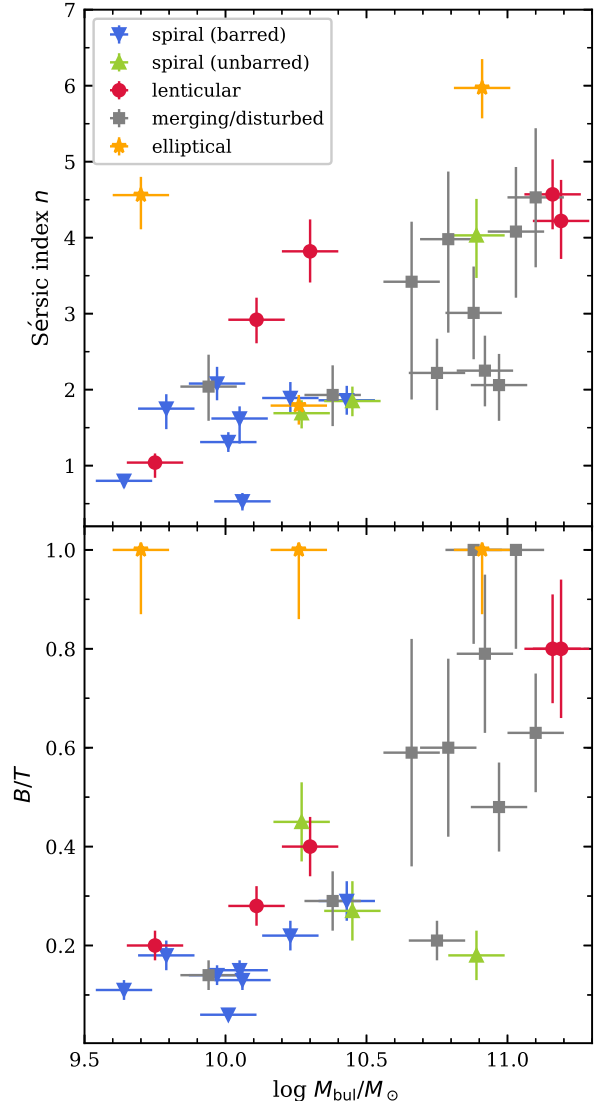


Figure 9. Dependence of bulge Sérsic index n (top) and B/T (bottom) with bulge stellar mass. The symbols are color-coded by morphological type of the host.

view, major external triggers are thought to be necessary to supply the high mass accretion rates needed to sustain the luminosities of the most powerful quasars (Shlosman et al. 1990). The less stringent fueling requirements of weaker AGNs can be met through internal secular processes, such as angular momentum transported by bars (e.g., Ho et al. 1997; Somerville et al. 2008; Hopkins & Hernquist 2009). A substantial body of observational evidence broadly supports this thesis. From their analysis of a large sample of AGNs spanning a wide range of bolometric luminosities and redshifts, Treister et al. (2012) report a strong correlation between the fraction of host galaxies experiencing major mergers and AGN luminosity. A high incidence of merger features is frequently found for luminous AGNs, be they unobscured

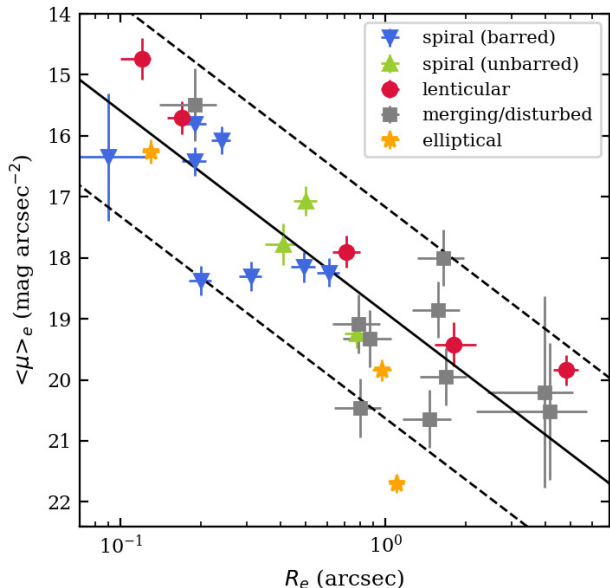


Figure 10. Kormendy relation for the bulges of the host galaxies, color-coded by morphological type. The solid line is the best-fit $\langle \mu \rangle_e - R_e$ relation for the bulges of elliptical, lenticular, and merging/disturbed galaxies, and the two dashed lines represent its $\pm 3\sigma$ scatter.

(e.g., Letawe et al. 2010; Liu et al. 2012; Hong et al. 2015), dust-reddened (Urrutia et al. 2008; Kocevski et al. 2015; Fan et al. 2016), or highly obscured (Villar-Martín et al. 2011; Bessiere et al. 2012; Wylezalek et al. 2016; Donley et al. 2018; Urbano-Mayorgas et al. 2018). But not everyone agrees. A significant number of studies of luminous AGNs at moderate ($0.5 < z < 0.8$; Villforth et al. 2014) and high ($z \lesssim 2$; Schawinski et al. 2011, 2012; Mechtley et al. 2016; Villforth et al. 2017) redshifts dismiss the importance of major mergers in driving nuclear activity.

One of the most surprising results of this study is the sheer diversity of the morphologies of the host galaxies of obscured quasars. As summarized in Section 1, the traditional gas-rich major merger scenario for quasar evolution predicts that type 2 quasars should be hosted by morphologically highly disturbed galaxies. This basic expectation is not supported by our observations, at least not for a sizable fraction of our sample. Among the 29 objects studied, only 10 (34%) show clear morphological signatures of interactions or mergers, rising at most to 13 (45%) if we regard the three ellipticals as post-merger products. The majority (55%; 11 spirals and 5 lenticulars) possess normal disks. Even if we accept that lenticulars may be remnants of major mergers (Eliche-Moral et al. 2018)—by no means a universal view (Kormendy et al. 2009)—a substantial fraction (38%) are incontrovertibly ordinary unbarred or barred late-

type spiral galaxies. Although it is stated that disks can survive from gas-rich major mergers under some circumstances (e.g., Barnes & Hernquist 1996; Springel & Hernquist 2005; Hopkins et al. 2009), the remnants cannot significantly fuel central black holes (Hopkins & Hernquist 2009), and the regrowth of the disk (Hopkins et al. 2009; Bundy et al. 2010) takes much longer than the typical quasar lifetime (e.g., Porciani et al. 2004; Hopkins et al. 2005; Shen et al. 2007). Therefore, the late-type host galaxies of type 2 quasars, which most likely possess pseudo bulges (Section 4.1), probably never experienced major mergers during their lifetimes. Secular processes presumably were responsible for their black hole growth. Interestingly, most of the spirals (8 out of 11) contain a bar (Figure 2).

The subset of our type 2 quasars hosted by spirals has a typical [O III] $\lambda 5007$ luminosity of $10^9 L_\odot$, not dissimilar from those hosted by earlier type galaxies or mergers. For an [O III] bolometric correction of 600 (Kauffmann & Heckman 2009), this corresponds to a bolometric luminosity of $L_{\text{bol}} = 2.3 \times 10^{45} \text{ erg s}^{-1}$, or a mass accretion rate of $\dot{M} = (\epsilon c^2)^{-1} L_{\text{bol}} \approx 0.4 M_\odot \text{ yr}^{-1}$, where c is the speed of light and $\epsilon = 0.1$ is the radiative efficiency. This level of fueling is modest, reflecting the fact that our sample of low-redshift obscured AGNs, although technically considered as “quasars”, are, in fact, quite modest in power. Bar-driven gravitational torques may suffice to transport cold gas at this rate to the central regions of spiral galaxies (Haan et al. 2009).

5. CONCLUSIONS

We observed 29 local ($z \approx 0.04 - 0.4$), optically selected type 2 quasars in rest-frame B and I using WFC3 on *HST*, to study the stellar properties of their host galaxies and explore their triggering mechanism. We classify the morphologies, perform detailed two-dimensional decomposition to study structural properties of the hosts, analyze their optical colors and color gradients, and derive bulge stellar masses. Our principal findings can be summarized as follows:

- Only a minority (34%) of the host galaxies exhibit clear merging or disturbed features. A significant fraction (38%) of the hosts are late-type, mostly disk-dominated spiral galaxies. Major mergers do not seem to play a dominant role in triggering nuclear activity in nearby obscured quasars, but the luminosities of these sources, and hence their mass accretion rates, are not sufficiently high to severely challenge the major merger model for quasar evolution. Indeed, we argue that secular processes alone may suffice to supply their modest fueling rates.
- The central regions of most of the host galaxies are bluer than their outer parts, indicating nearly

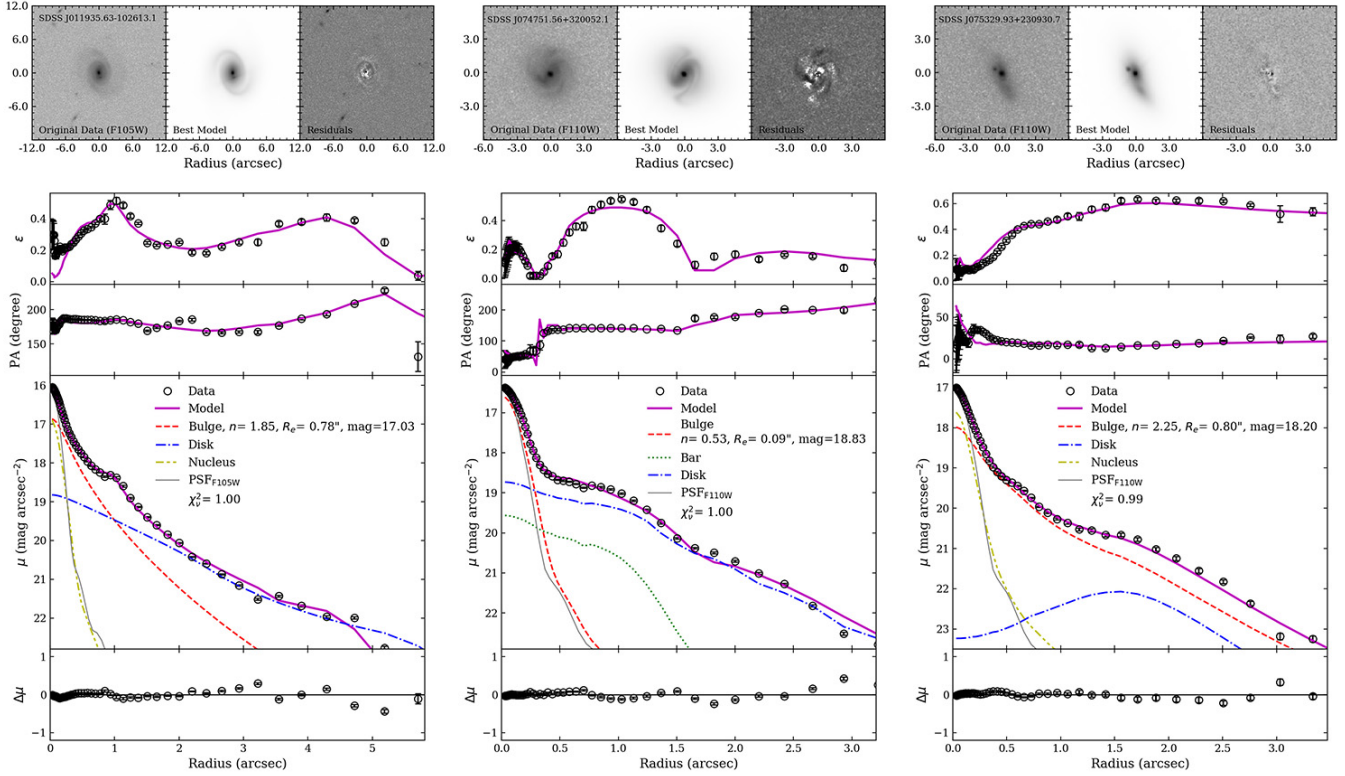


Figure A1: GALFIT decompositions for the 29 type 2 quasars. For each object, the top row shows (left) the observed I_{WFC3} image, (middle) the best-fit 2-D model, and (right) the residual image. The bottom panels give, respectively, the radial profile of ellipticity, position angle, surface brightness, are the residuals between the best-fit model and the observed surface brightness profile. The best-fit 1-D model (magenta line) was extracted from the best-fit 2-D model. The individual subcomponents are listed in the legend, which also gives the final reduced chi-squared of the fit. The profile for the PSF is plotted as a gray line.

ubiquitous recent or ongoing star formation.

- While merging/disturbed systems and early-type (lenticular and elliptical) hosts tend to have Sérsic indices ($n \geq 2$) and bulge-to-total ratios ($B/T \gtrsim 0.2$) expected of classical bulges, the late-type hosts possess pseudo bulges with $n < 2$ and $B/T \lesssim 0.2$. However, unlike inactive galaxies, the pseudo bulges hosting type 2 quasars have systematically higher central surface brightnesses because of the excess light from young stars.

We thank an anonymous referee for many helpful comments. We are grateful to MinZhi Kong and Hua Gao for fruitful discussions and suggestions. This work was supported by the National Key R&D Program of China (2016YFA0400702) and the National Science Foundation of China (11473002, 11721303). Minjin Kim was supported by the National Research Foundation of Korea (NRF) grant funded by the Korea government (MSIT) (No. 2017R1C1B2002879).

APPENDIX

A. BEST-FIT DECOMPOSITIONS FOR THE SAMPLE

Here are the best-fit results of structure decomposition for the host galaxies of our 29 type 2 quasar by GALFIT. For each quasar, the 2-D original I_{WFC3} image, model, and residual images are illustrated in the upper panel, and the 1-D distributions of ellipticity, position angle, surface density, and residual of intensity along with radius are shown in the bottom panel.

REFERENCES

- Adelman-McCarthy, J. K., Agüeros, M. A., Allam, S. S., et al. 2008, *ApJS*, 175, 297
- Alexander, D. M., & Hickox, R. C. 2012, *New A Rev.*, 56, 93

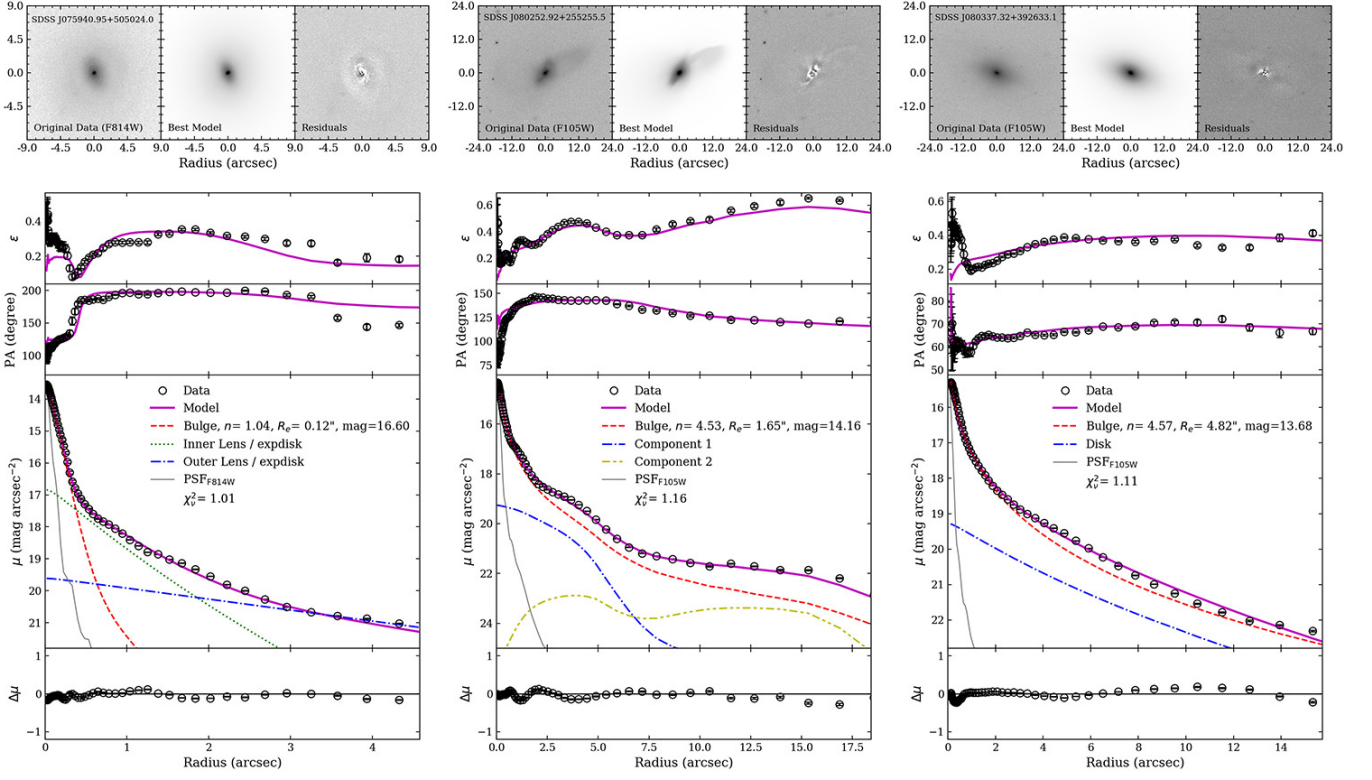


Figure A1 (Cont.): GALFIT decompositions for type 2 quasars.

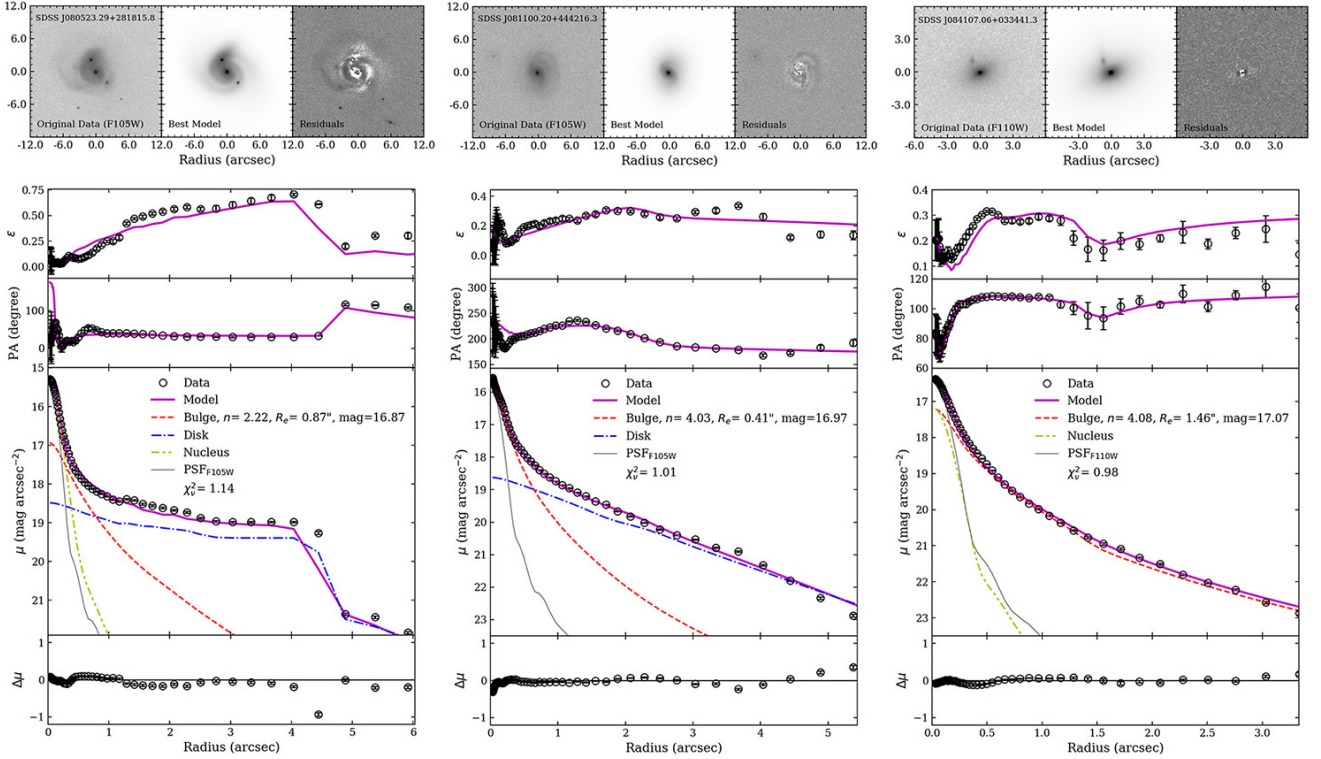


Figure A1 (Cont.): GALFIT decompositions for type 2 quasars.

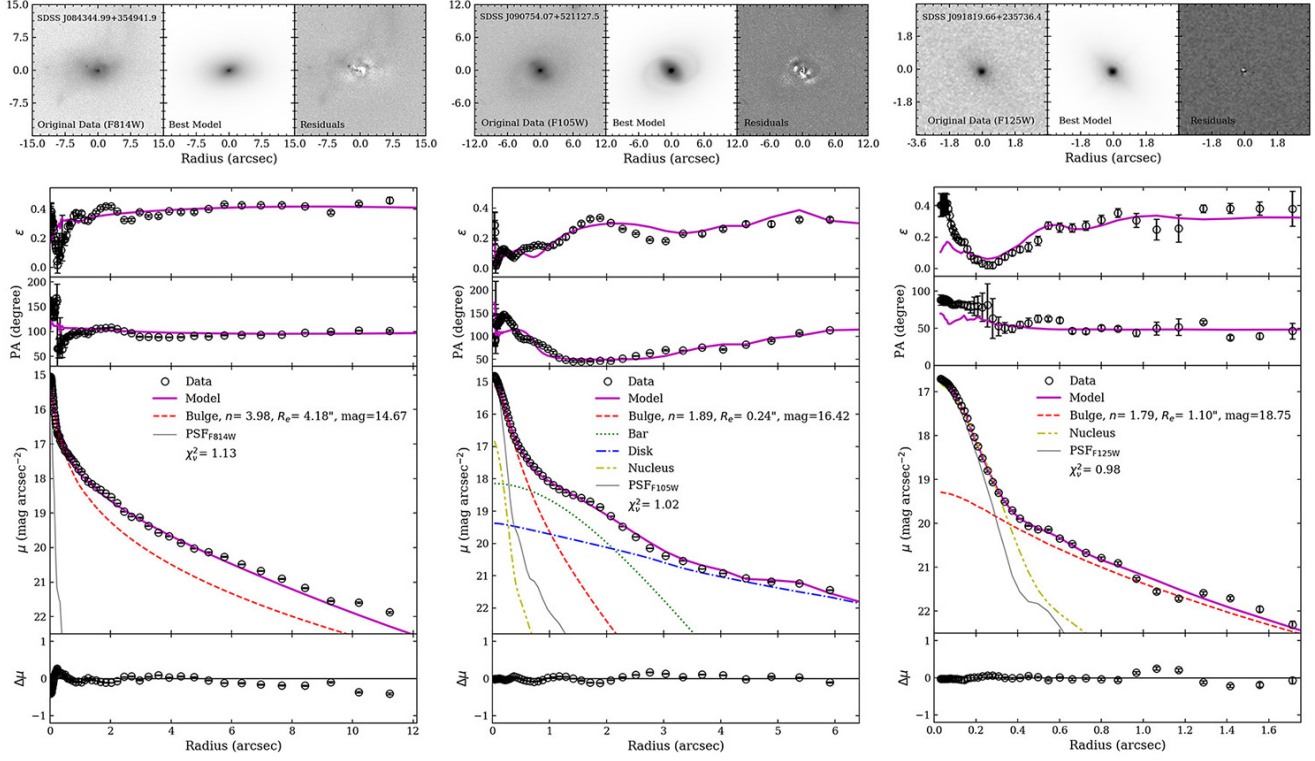


Figure A1 (Cont.): GALFIT decompositions for type 2 quasars.

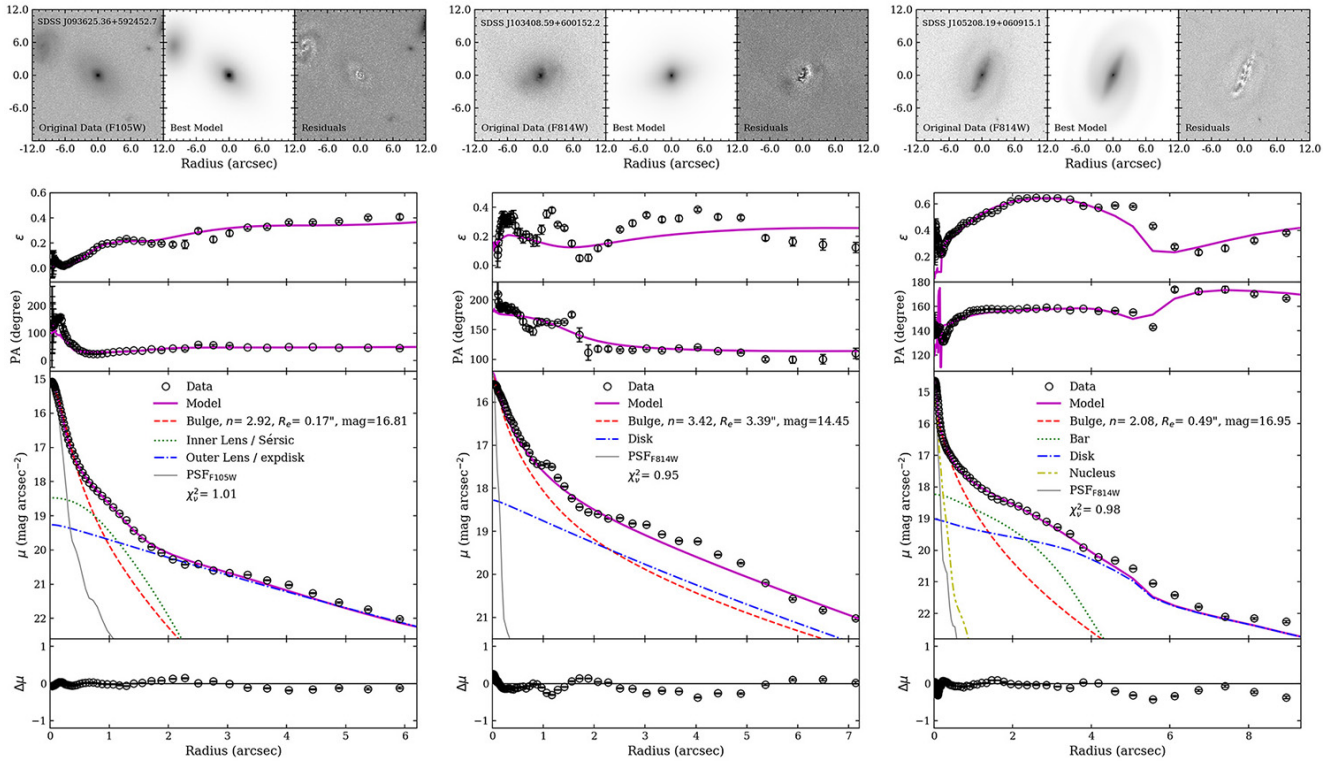


Figure A1 (Cont.): GALFIT decompositions for type 2 quasars.

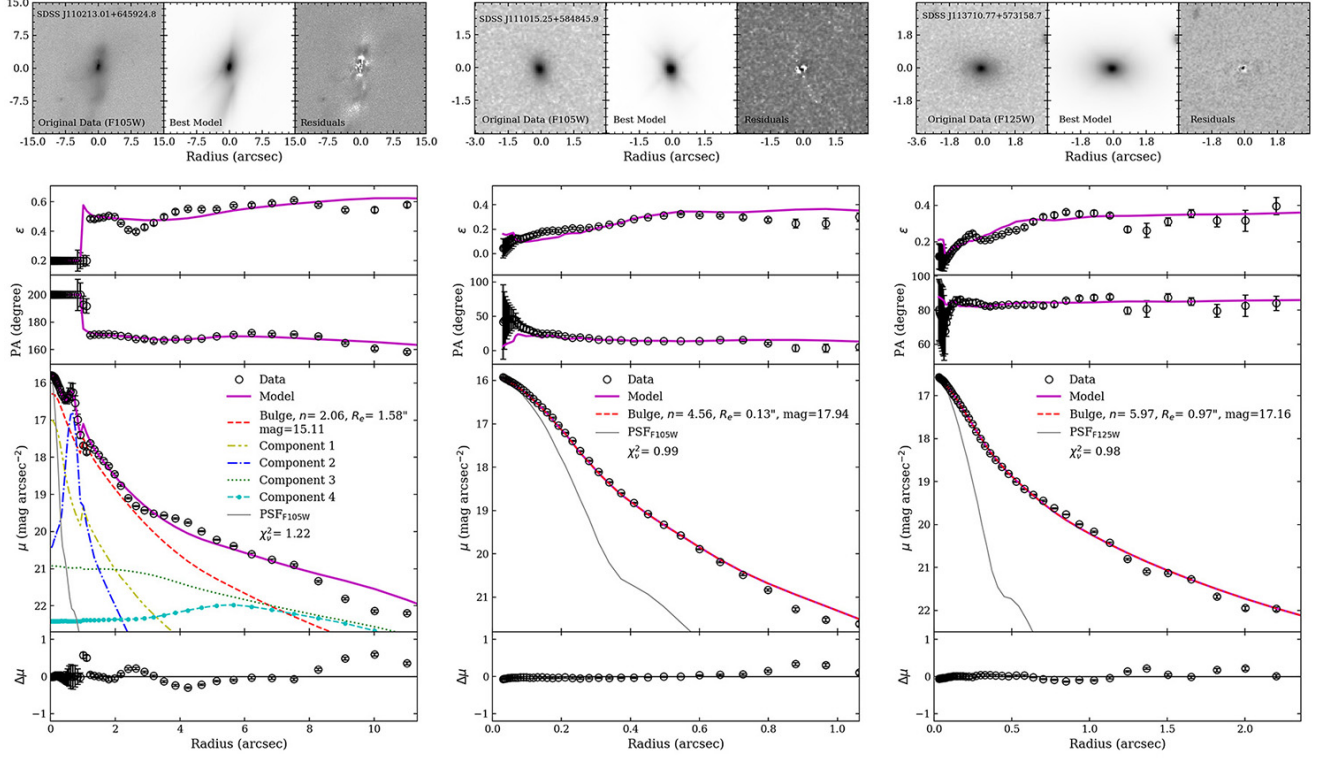


Figure A1 (Cont.): GALFIT decompositions for type 2 quasars.

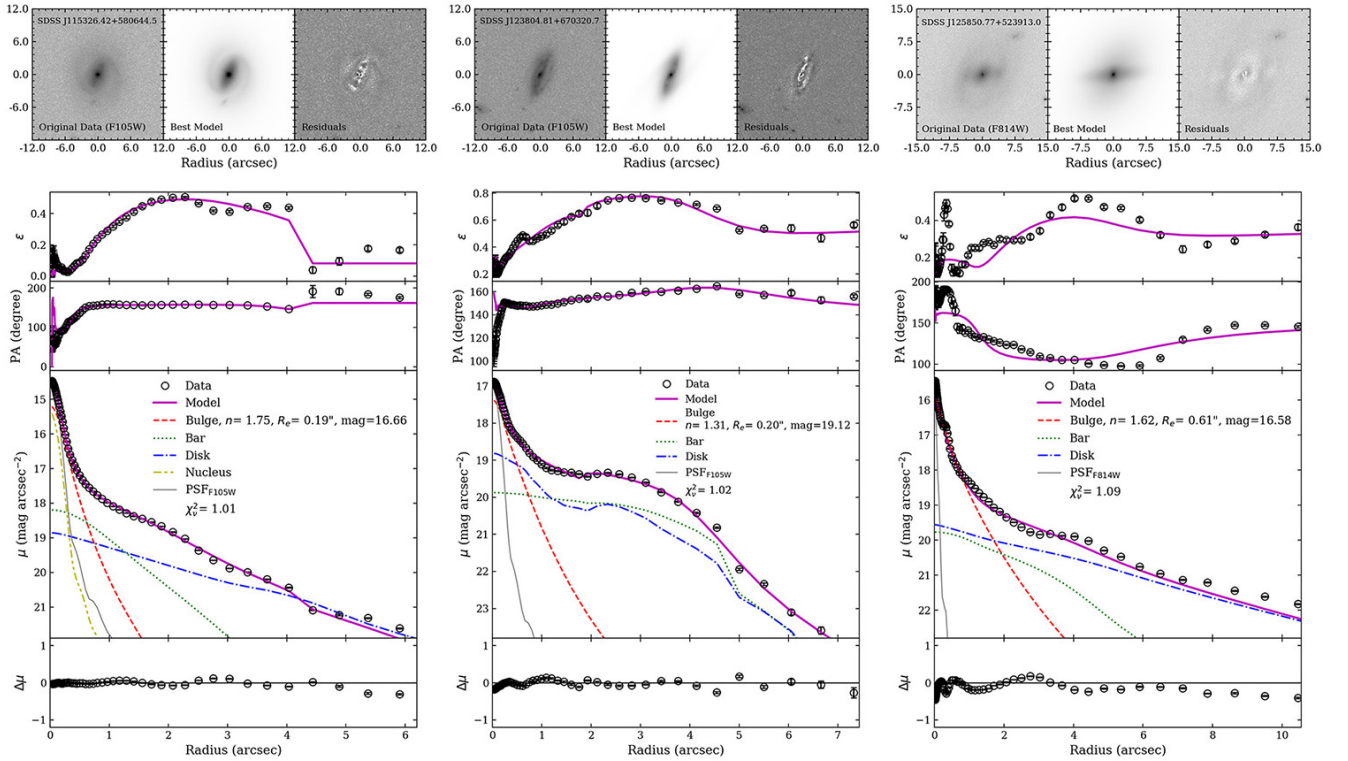


Figure A1 (Cont.): GALFIT decompositions for type 2 quasars.

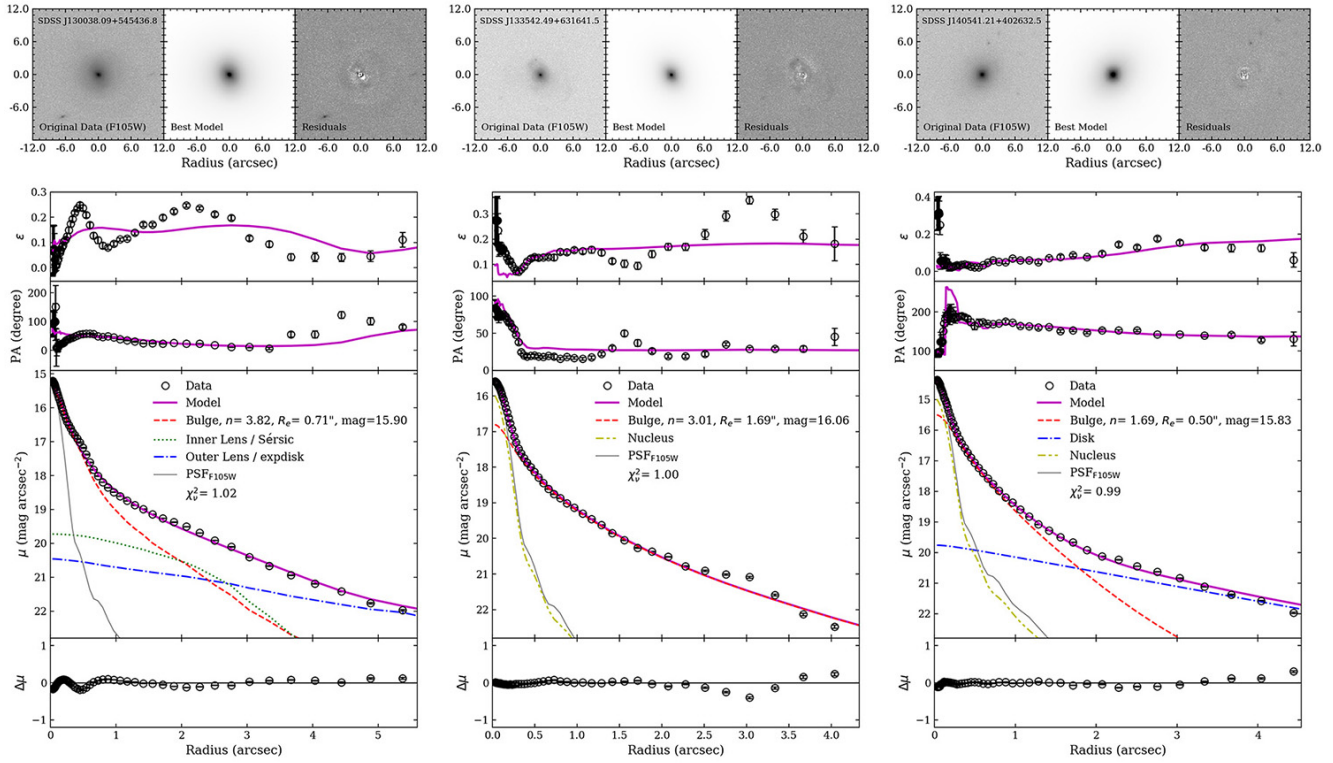


Figure A1 (Cont.): GALFIT decompositions for type 2 quasars.

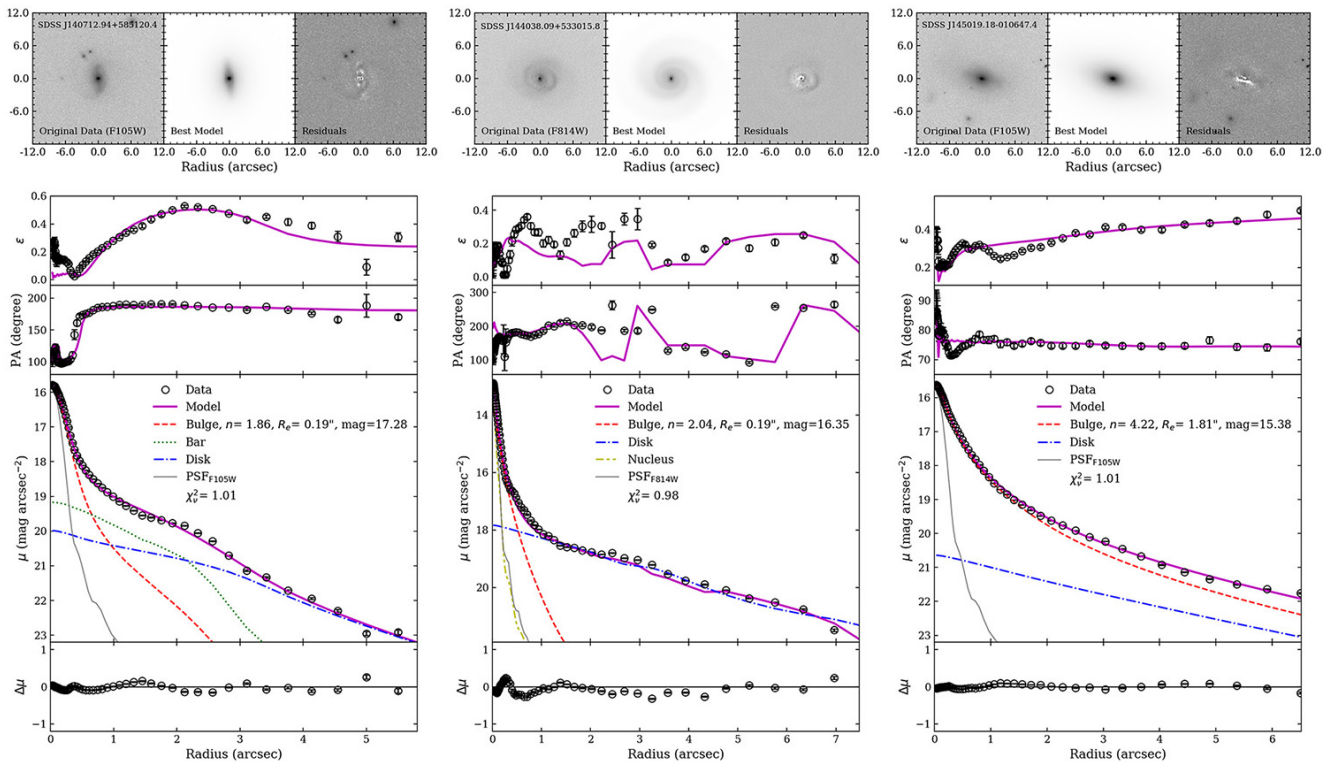


Figure A1 (Cont.): GALFIT decompositions for type 2 quasars.

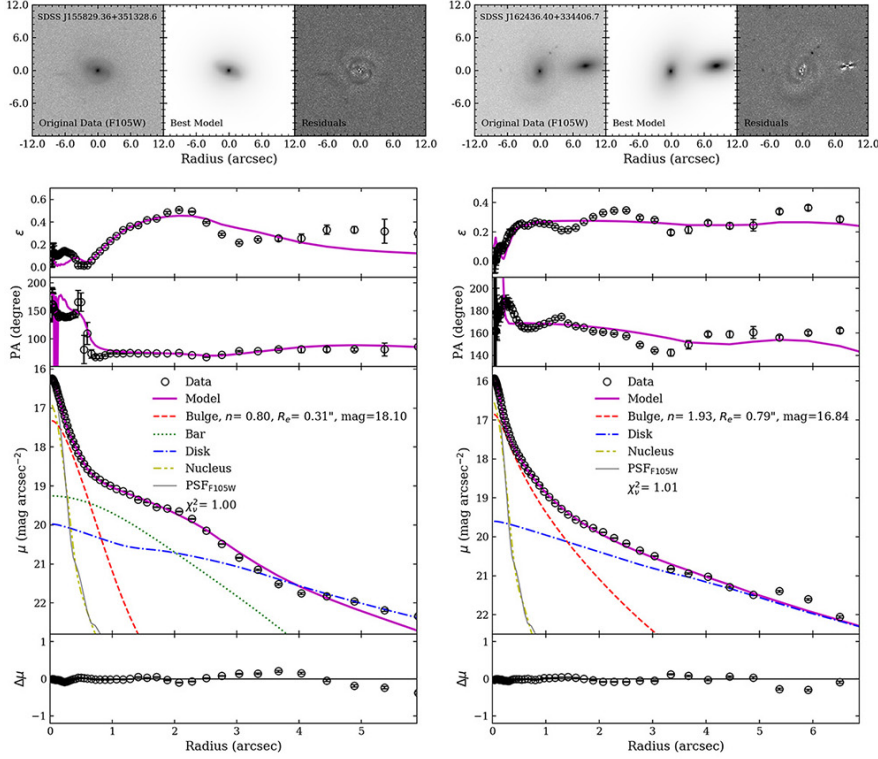


Figure A1 (Cont.): GALFIT decompositions for type 2 quasars.

- Alexandroff, R. M., Zakamska, N. L., van Velzen, S., Greene, J. E., & Strauss, M. A. 2016, *MNRAS*, 463, 3056
- Antonucci, R. R. J., & Miller, J. S. 1985, *ApJ*, 297, 621
- Balcells, M., Graham, A. W., Domínguez-Palmero, L., & Peletier, R. F. 2003, *ApJL*, 582, L79
- Barden, M., Häußler, B., Peng, C. Y., McIntosh, D. H., & Guo, Y. 2012, *MNRAS*, 422, 449
- Barden, M., Jahnke, K., & Häußler, B. 2008, *ApJS*, 175, 105
- Barnes, J. E., & Hernquist, L. 1996, *ApJ*, 471, 115
- Bell, E. F., & de Jong, R. S. 2001, *ApJ*, 550, 212
- Bell, E. F., McIntosh, D. H., Katz, N., & Weinberg, M. D. 2003, *ApJS*, 149, 289
- Bennett, C. L., Larson, D., Weiland, J. L., & Hinshaw, G. 2014, *ApJ*, 794, 135
- Bertin, E., & Arnouts, S. 1996, *A&AS*, 117, 393
- Bessiere, P. S., Tadhunter, C. N., Ramos Almeida, C., & Villar Martín, M. 2012, *MNRAS*, 426, 276
- . 2014, *MNRAS*, 438, 1839
- Bessiere, P. S., Tadhunter, C. N., Ramos Almeida, C., Villar Martín, M., & Cabrera-Lavers, A. 2017, *MNRAS*, 466, 3887
- Binney, J., & Merrifield, M. 1998, *Galactic Astronomy*
- Böker, T., Laine, S., van der Marel, R. P., et al. 2002, *AJ*, 123, 1389
- Boroson, T. A., & Green, R. F. 1992, *ApJS*, 80, 109
- Bruzual, G., & Charlot, S. 2003, *MNRAS*, 344, 1000
- Bundy, K., Scarlata, C., Carollo, C. M., et al. 2010, *ApJ*, 719, 1969
- Canalizo, G., & Stockton, A. 2013, *ApJ*, 772, 132
- Cardelli, J. A., Clayton, G. C., & Mathis, J. S. 1989, *ApJ*, 345, 245
- Cisternas, M., Jahnke, K., Inskip, K. J., et al. 2011, *ApJ*, 726, 57
- Conroy, C., Gunn, J. E., & White, M. 2009, *ApJ*, 699, 486
- de Jong, R. S. 1996, *A&AS*, 118, 557
- Di Matteo, T., Springel, V., & Hernquist, L. 2005, *Nature*, 433, 604
- Dicken, D., Tadhunter, C., Morganti, R., et al. 2014, *ApJ*, 788, 98
- Donley, J. L., Kartaltepe, J., Kocevski, D., et al. 2018, *ApJ*, 853, 63
- Dunlop, J. S., McLure, R. J., Kukula, M. J., et al. 2003, *MNRAS*, 340, 1095
- Eliche-Moral, M. C., Rodríguez-Pérez, C., Borlaff, A., Querejeta, M., & Tapia, T. 2018, *A&A*, 617, A113
- Fan, L., Han, Y., Fang, G., et al. 2016, *ApJL*, 822, L32
- Ferrarese, L., & Merritt, D. 2000, *ApJL*, 539, L9
- Fisher, D. B., & Drory, N. 2008, *AJ*, 136, 773
- . 2010, *ApJ*, 716, 942
- Floyd, D. J. E., Kukula, M. J., Dunlop, J. S., et al. 2004, *MNRAS*, 355, 196
- Freeman, K. C. 1966, *MNRAS*, 133, 47
- Gadotti, D. A. 2008, *MNRAS*, 384, 420
- . 2009, *MNRAS*, 393, 1531
- Gao, H., & Ho, L. C. 2017, *ApJ*, 845, 114
- Gao, H., Ho, L. C., Barth, A. J., & Li, Z.-Y. 2018, *ApJ*, 862, 100
- . 2019, *ApJS*, submitted
- Gebhardt, K., Bender, R., Bower, G., et al. 2000, *ApJL*, 539, L13
- Greene, J. E., Ho, L. C., & Barth, A. J. 2008, *ApJ*, 688, 159
- Haan, S., Schinnerer, E., Emsellem, E., et al. 2009, *ApJ*, 692, 1623
- Heckman, T. M., Ptak, A., Hornschemeier, A., & Kauffmann, G. 2005, *ApJ*, 634, 161
- Ho, L. C., Filippenko, A. V., & Sargent, W. L. W. 1997, *ApJ*, 487, 591
- Ho, L. C., Li, Z.-Y., Barth, A. J., Seigar, M. S., & Peng, C. Y. 2011, *ApJS*, 197, 21
- Hong, J., Im, M., Kim, M., & Ho, L. C. 2015, *ApJ*, 804, 34
- Hopkins, P. F., Cox, T. J., Younger, J. D., & Hernquist, L. 2009, *ApJ*, 691, 1168

- Hopkins, P. F., & Hernquist, L. 2009, *ApJ*, 694, 599
- Hopkins, P. F., Hernquist, L., Cox, T. J., et al. 2005, *ApJ*, 630, 705
- Hopkins, P. F., Hernquist, L., Cox, T. J., & Kereš, D. 2008, *ApJS*, 175, 356
- Hopkins, P. F., Kocevski, D. D., & Bundy, K. 2014, *MNRAS*, 445, 823
- Hopkins, P. F., Somerville, R. S., Hernquist, L., et al. 2006, *ApJ*, 652, 864
- Huang, S., Ho, L. C., Peng, C. Y., Li, Z.-Y., & Barth, A. J. 2013, *ApJ*, 766, 47
- Ilbert, O., Tresse, L., Zucca, E., et al. 2005, *A&A*, 439, 863
- Jiang, Y.-F., Greene, J. E., Ho, L. C., Xiao, T., & Barth, A. J. 2011, *ApJ*, 742, 68
- Jogee, S. 2006, in *Lecture Notes in Physics*, Berlin Springer Verlag, Vol. 693, *Physics of Active Galactic Nuclei at all Scales*, ed. D. Alloin, 143
- Kauffmann, G., & Heckman, T. M. 2009, *MNRAS*, 397, 135
- Kim, M., & Ho, L. C. 2019, arXiv e-prints, arXiv:1903.08796
- Kim, M., Ho, L. C., Peng, C. Y., Barth, A. J., & Im, M. 2008a, *ApJS*, 179, 283
- . 2017, *ApJS*, 232, 21
- Kim, M., Ho, L. C., Peng, C. Y., et al. 2008b, *ApJ*, 687, 767
- Kocevski, D. D., Brightman, M., Nandra, K., et al. 2015, *ApJ*, 814, 104
- Kong, M., & Ho, L. C. 2018, *ApJ*, 859, 116
- Kormendy, J. 1977, *ApJ*, 218, 333
- Kormendy, J., Fisher, D. B., Cornell, M. E., & Bender, R. 2009, *ApJS*, 182, 216
- Kormendy, J., & Ho, L. C. 2013, *ARA&A*, 51, 511
- Kormendy, J., & Kennicutt, Jr., R. C. 2004, *ARA&A*, 42, 603
- Krist, J. E., Hook, R. N., & Stoehr, F. 2011, in *Proc. SPIE*, Vol. 8127, *Optical Modeling and Performance Predictions V*, 81270J
- Kron, R. G. 1980, *ApJS*, 43, 305
- Kroupa, P. 2001, *MNRAS*, 322, 231
- LaMassa, S. M., Heckman, T. M., Ptak, A., et al. 2009, *ApJ*, 705, 568
- Laurikainen, E., Salo, H., & Buta, R. 2005, *MNRAS*, 362, 1319
- Laurikainen, E., Salo, H., Buta, R., & Vasylyev, S. 2004, *MNRAS*, 355, 1251
- Letawe, Y., Letawe, G., & Magain, P. 2010, *MNRAS*, 403, 2088
- Li, Z.-Y., Ho, L. C., Barth, A. J., & Peng, C. Y. 2011, *ApJS*, 197, 22
- Liu, X., Shen, Y., & Strauss, M. A. 2012, *ApJ*, 745, 94
- Magorrian, J., Tremaine, S., Richstone, D., et al. 1998, *AJ*, 115, 2285
- Martínez-Sansigre, A., Rawlings, S., Lacy, M., et al. 2005, *Nature*, 436, 666
- Martini, P. 2004, *Coevolution of Black Holes and Galaxies*, 169
- Martini, P., & Weinberg, D. H. 2001, *ApJ*, 547, 12
- Mehtley, M., Jahnke, K., Windhorst, R. A., et al. 2016, *ApJ*, 830, 156
- Peng, C. Y., Ho, L. C., Impey, C. D., & Rix, H.-W. 2002, *AJ*, 124, 266
- . 2010, *AJ*, 139, 2097
- Porciani, C., Magliocchetti, M., & Norberg, P. 2004, *MNRAS*, 355, 1010
- Ramos Almeida, C., Tadhunter, C. N., Inskip, K. J., et al. 2011, *MNRAS*, 410, 1550
- Ramos Almeida, C., Bessiere, P. S., Tadhunter, C. N., et al. 2012, *MNRAS*, 419, 687
- Reyes, R., Zakamska, N. L., Strauss, M. A., et al. 2008, *AJ*, 136, 2373
- Schawinski, K., Simmons, B. D., Urry, C. M., Treister, E., & Glikman, E. 2012, *MNRAS*, 425, L61
- Schawinski, K., Treister, E., Urry, C. M., et al. 2011, *ApJL*, 727, L31
- Schmidt, M., & Green, R. F. 1983, *ApJ*, 269, 352
- Sérsic, J. L. 1968, *Atlas de Galaxias Australes*
- Shen, Y., Mulchaey, J. S., Raychaudhury, S., Rasmussen, J., & Ponman, T. J. 2007, *ApJL*, 654, L115
- Shlosman, I., Begelman, M. C., & Frank, J. 1990, *Nature*, 345, 679
- Somerville, R. S., Hopkins, P. F., Cox, T. J., Robertson, B. E., & Hernquist, L. 2008, *MNRAS*, 391, 481
- Springel, V., Di Matteo, T., & Hernquist, L. 2005, *ApJL*, 620, L79
- Springel, V., & Hernquist, L. 2005, *ApJL*, 622, L9
- Tadhunter, C., Holt, J., González Delgado, R., et al. 2011, *MNRAS*, 412, 960
- Treister, E., Schawinski, K., Urry, C. M., & Simmons, B. D. 2012, *ApJL*, 758, L39
- Urbano-Mayorgas, J. J., Villar Martín, M., Buitrago, F., et al. 2018, *MNRAS*, arXiv:1810.11240
- Urrutia, T., Lacy, M., & Becker, R. H. 2008, *ApJ*, 674, 80
- Veilleux, S., Kim, D.-C., Rupke, D. S. N., et al. 2009, *ApJ*, 701, 587
- Vika, M., Vulcani, B., Bamford, S. P., Häußler, B., & Rojas, A. L. 2015, *A&A*, 577, A97
- Villar-Martín, M., Cabrera Lavers, A., Bessiere, P., et al. 2012, *MNRAS*, 423, 80
- Villar-Martín, M., Tadhunter, C., Humphrey, A., et al. 2011, *MNRAS*, 416, 262
- Villforth, C., Hamann, F., Rosario, D. J., et al. 2014, *MNRAS*, 439, 3342
- Villforth, C., Hamilton, T., Pawlik, M. M., et al. 2017, *MNRAS*, 466, 812
- Wild, V., Heckman, T., & Charlot, S. 2010, *MNRAS*, 405, 933
- Wylezalek, D., Zakamska, N. L., Liu, G., & Obied, G. 2016, *MNRAS*, 457, 745
- York, D. G., Adelman, J., Anderson, Jr., J. E., et al. 2000, *AJ*, 120, 1579
- Yu, Q., & Tremaine, S. 2002, *MNRAS*, 335, 965
- Zakamska, N. L., Strauss, M. A., Krolik, J. H., et al. 2003, *AJ*, 126, 2125
- . 2006, *AJ*, 132, 1496